
TREE NETWORKS OF REAL-WORLD DATA: ANALYSIS OF EFFICIENCY AND SPATIOTEMPORAL SCALES

A PREPRINT

Davide Cipollini^{*,1,2}, **Lambert Schomaker**^{1,2}

¹ Bernoulli Institute for Mathematics, Computer Science and Artificial Intelligence,
University of Groningen, Nijenborgh 9, 9747 AG Groningen, The Netherlands

² Cognigron - Groningen Cognitive Systems and Materials Center,
Nijenborgh 9, 9747 AG Groningen, The Netherlands

*Corresponding author: Davide Cipollini Email: d.cipollini@rug.nl

ABSTRACT

This work computationally investigates an algorithm that was originally proposed for creating and searching trees of patterns under the assumption that it seeks the most efficient internal representation of the external world, namely a real-world dataset of patterns. The algorithm produces a transition from star graph to regular 1d lattice, passing through irregular scale-invariant trees, under the effect of a single control parameter. The relatively novel information-theoretic tools of the von Neumann entropy and its derivative, the specific heat, together with the recent definition of thermodynamic quantities, such as work and heat, for networks are reviewed and applied to inspect the tree structures produced by the formation protocol. We observe some consistency between the optimal thermodynamic efficiency for networks and the optimal pattern-matching efficiency, defined in terms of the trade-off between accuracy and computational cost when the former is measured at the meso-resolution scale involved in the phase transition from star graph to scale-invariant network. We adduce the hypothesis of a richer frequency content at the meso-scale of the self-organized network to explain this observation. Moreover, empirical evidence suggests that the system benefits from the vicinity to the mentioned phase transition if it is faced with higher-complexity environments, while it does not when the environment is simpler. A phase portrait of the tree-generating algorithm is provided and multiple phase transitions are identified.

Keywords Trees · Networks · Thermodynamics · Statistical physics · Machine Learning · von Neumann entropy · Specific heat

1 Introduction

Why complex structures emerge in a real-world environment is a fascinating question that has not yet found a fully satisfactory answer. In a recent article [1], the emergence of complex structures is devised as the macroscopic thermodynamic result of the optimal ability to store the information about the environment in an accessible manner with the ability to transmit information across the structure [2]. The latter is defined in terms of microscopic quantities thanks to the fairly new developments in statistical physics in network theory [1, 3, 4, 5]. In living systems, natural selection is the way the information about the environment flows into the system's genome which will then encode such information in the structural traits of the organisms which in turn reflect the functional capability of the system. Thus, the structural traits of a system could themselves enclose the complexity of the environmental conditions the system needs to adapt to, or in other words, to represent into its very own structure [6]. How these traits are optimized to maximize the fitness to the environment is an open question. The hypothesis of optimal functioning at the border of order and disorder suggests the critical point as the potential candidate to obtain functional advantages [7, 8, 9, 10, 11] and maximize the fitness to the outer world, or to obtain a better performance in a statistical generalization problem

in the context of learning machines. Here we challenge this hypothesis. In our work, a system seeks the best-fitness configuration given some external constraints r and a high-dimensional vector collection, the dataset \mathcal{D} .

We take as a case study the algorithm introduced by Portegys [12] for accelerating nearest-neighbor (1-NN) pattern recognition tasks and subsequently extended to k-NN [13]. The algorithm employs a tree-formation protocol where raw data are reorganized into hierarchical tree structures using a recursive tree-formation method in which samples are randomly selected and inserted into the growing network. At each step, the new pattern is linked to either the current parent pattern or to one of the k-NN children of the parent pattern. The choice is based on the distance between the parent and the new pattern and the one evaluated between the child pattern and the new pattern. The parameter r modulates the relative importance of these two distances creating a larger or smaller region of influence of the parent in the sample space. Figure 1 shows the three structure prototypes produced depending on the value of the control parameter r . For $r \sim 0$, every node is linked to the root node (see the central node, which is the first node selected in the process) and a star graph turns out. For some intermediate value of r a ragged tree structure with progressively smaller distances between the patterns is produced, while for $r \rightarrow 2$ a 1d-lattice is created. The algorithm produces exclusively trees, i.e. loop-less networks, which are necessarily sparse $|E| = N - 1$ where $|E|$ and N are the number of links and nodes respectively. Using the metaphor introduced by Jacob for natural selection [14], the algorithm does act as a *tinkerer* that creates a structure using what is available at the time, collocating one node after the other across the tree formation process according to a parameterized distance-based rule.

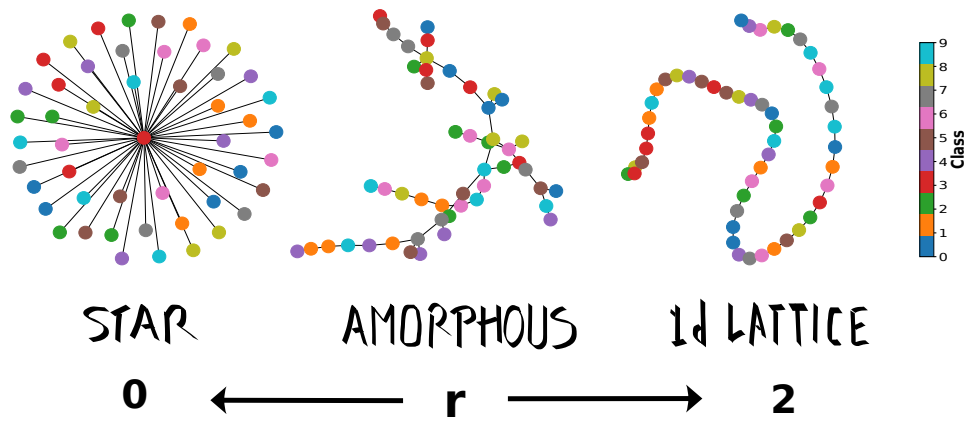


Figure 1: **Tree structures generated by the Portegys algorithm.** The algorithm creates star-like networks up to 1d lattice when $r \rightarrow 2$. For intermediate values of r , networks resembling an arborescent tree are produced. The process is reminiscent of the transition *vapor/liquid* \rightarrow *amorphous solid* \rightarrow *1d lattice*. Depicted networks are generated from a subset of 50 samples randomly extracted from the MNIST dataset with $r = 0.05, 0.95, 1.50$ respectively. Classes are indicated by the 10 different colors in the color bar.

The use of a hierarchical topology, onto which a high-dimensional dataset is mapped, offers insights into the structured disorder of the data [15] on the one hand, while on a practical perspective, it limits the number of comparisons needed in matching an unknown pattern to a prototypical example. Namely, the algorithm introduced by Portegys is equipped with a pattern-searching method described in Section 3.1. Depending on the structural traits of the networks, an optimal trade-off between fast search of the best-matching pattern and accuracy in terms of node-class labels can be defined.

The Portegys algorithm has the desirable properties of being simple, explainable, and subject to a single control parameter r . Thanks to these features, we can work on the bridge between three disciplines: statistical physics, machine learning, and network science, and we can show that information-theoretical tools such as the von Neumann entropy and its derivative reflect the functional capabilities of the network. Notably, we observe some consistency between the thermodynamic efficiency and pattern-matching efficiency that we try to explain in terms of average frequency content in the self-organized network structure.

2 Theoretical framework

2.1 Statistical physics of networks

Information spreading over networked structures is governed by the Laplacian matrix [16] and its spectrum of eigenvalues encodes many relevant topological properties of the graph [17, 18]. Let us consider an undirected and unweighted network $G(V, E)$ of order $|V| = N$ with the number of links equal to $|E| = m$. The network Laplacian is defined as $\hat{L} = \hat{D} - \hat{A}$, where \hat{D} and \hat{A} are the diagonal matrix of the node degrees and the adjacency matrix respectively. The Laplacian operator can be used to define a density operator [5], where the Laplacian takes the role of the Hamiltonian of statistical physics [19] as in Equation (1).

Given an initial state of the network encoding the concentration of a quantity, e.g. information, in one or more nodes, $\underline{s}(0)$, the state at time τ is given by $\underline{s}(\tau) = e^{-\tau\hat{L}}\underline{s}(0)$. Where $\hat{K} = e^{-\tau\hat{L}}$ is the network propagator and is the discrete counterpart of the path integral formulation for general diffusion processes [20, 21].

As \hat{K} is a positive semidefinite Hermitian matrix admits the spectral decomposition in terms of the sum of projectors $\hat{K} = \sum_i^N e^{-\tau\lambda_i} |k_i\rangle\langle k_i|$. Thus, for any state at τ it holds $|\phi(\tau)\rangle = \sum_i^N e^{-\tau\lambda_i} |k_i\rangle\langle k_i| |\phi(0)\rangle$. This relation remarks that the eigenvectors of the Laplacian are akin to the wave vectors in the Fourier space defined by the spectrum of the continuum-Laplacian, while τ can be interpreted as the "wavelength" $l \sim \tau$ of the diffusion modes, thus it defines an operational resolution scale for observations [3]. Moreover, the ensemble of accessible diffusion modes at time τ can be constructed by defining a probability measure over the accessible modes decomposed by the spectral theorem. Such canonical ensemble [5, 4, 22] is encoded into the density matrix:

$$\hat{\rho}(\tau) = \frac{e^{-\tau\hat{L}}}{Z} \quad (1)$$

The elements ρ_{ij} represent the normalized amount of information transferred in a diffusion process between nodes i and j at time τ . Remarkably ρ_{ij} takes into account all possible topological pathways between the two nodes and assigns smaller weights to longer ones tantamount to path-integrals [20, 22]. The partition function $Z = \text{Tr}[\hat{K}] = \sum_{i=1}^N e^{-\tau\lambda_i(\hat{L})}$ is a function of the eigenvalues, λ_i , of the Laplacian and is proportional to the average return probability of a continuous time edge-centric random walker to be back in its initial location after time τ [4]. Note that the object $\hat{\rho}$ is a positive semi-definite and Hermitian matrix whose trace sums to unity which has allowed its eigenvalues to be interpreted as probabilities.

Finally, the von Neumann spectral entropy can be introduced [5] as a multi-scale descriptor of the network structure:

$$S(\hat{\rho}(\tau)) = - \sum_{i=1}^N \mu_i(\tau) \log \mu_i(\tau) \quad (2)$$

where $\{\mu_i(\tau)\}_{i=1}^N$ is the set of $\hat{\rho}(\tau)$ eigenvalues that are related to the set of Laplacian eigenvalues through $\mu_i(\tau) = e^{-\tau\lambda_i}/Z$. The entropy $S(\hat{\rho}(\tau))$ is a function of the normalized time τ and is bounded between $[\log C_{conn}, \log N]$ where C_{conn} is the number of connected components and N is the number of nodes. Thus the von Neumann entropy, S , as a function of τ reflects the *entropic phase transition* of information propagation (or loss) over the network [22]. Specifically for a connected network, at $\tau \rightarrow 0$, $S(\tau) = \log N$ reflects the segregated heterogeneous phase where information diffuses from the single nodes to the very local neighborhood; at $\tau \rightarrow \infty$, $S(\tau) = 0$ the diffusion is governed by the smallest non-zero eigenvalue of the Laplacian, associated with the so-called Fiedler eigenvector, reflecting the integrated homogeneous phase where the information has propagated all over the network.

The network entropy thus counts the (logarithmic) number of informationally unconnected nodes in the heterogeneous network and by the inspection of the entropy S and its generalized susceptibility (or specific heat), $C = -dS/d \log \tau$, it is possible to identify the characteristic resolution scales of the network [22, 3]. For instance, a single large peak of the specific heat C identifies a single scale where there is a fast and unique information diffusion (or information lost) across the network. The latter is the typical situation of a star graph, depicted in Figure 1, or an Erdős-Rényi network. Before the peak, the informationally connected components are the single nodes, while after the peak the informationally connected components are the full network revealing a single trivial scale. On the contrary, a constant specific heat reflects the scale-invariance of the network in a resolution region where information is lost at a constant rate. Such a situation is typical of homogeneous d -dimensional lattices and of heterogeneous networks whose spectral density is power-law distributed in a sufficiently extended scale-interval [3]. The latter sentence makes for a definition for the scale-invariant networks [23]. The specific heat plateau height, C_0 , is also related to the spectral dimension of the network $d_s = 2C_0$ [3, 23].

From these considerations, a Laplacian-Renormalization group theory has been recently developed allowing for a coarse-graining of the network structures into super-nodes unraveling the mesoscale structures [3, 22]. In this context, the peaks of the specific heat, C , or a marked change in its slope, identify the most convenient resolution scales where to perform the coarse-graining over the *informationally connected* nodes, as it allows the iteration of the procedure without an excessive network reduction, and, when the network is scale-invariant, maintaining the dilation symmetry across the renormalization group procedure [19].

To conclude, we can intuitively use the diffusion parameter τ to resolve the network topological structures at different resolution scales. Thus, the necessity of analyzing complex networked systems at all levels is solved by resorting to the conjugate Fourier space, the k -space, defined by the Laplacian spectrum and the "wavelengths" of its modes.

2.2 Thermodynamics of networks

The statistical physics theory for networks introduced above allows us to view network phenomena from a new perspective and possibly to bridge the gap to network macroscopic observables. To this regard network thermodynamic quantities such as work, W , and heat, Q , have been defined in mathematical analogy to their thermodynamic counterparts [1]. Since a network of isolated nodes is the only network with maximum entropy $S_{iso} = \log N$ for $\tau > 0$, progressively adding edges diminishes the network's entropy. Where lower entropy reflects the diminished ability of the network to express diversity to a stochastic perturbation, or in other terms, the loss in the internal representation capabilities encoded in the network topological traits. The entropic cost is given by:

$$Q = -\frac{\delta S}{\tau} = -\frac{\log N - S}{\tau} \leq 0 \quad (3)$$

which mathematically resembles the heat dissipation in a thermodynamic process.

On the other hand, adding edges increases the gain in information flow quantified by the (Helmholtz) free energy $F = -\log Z/\tau$ [1, 4]. Less obvious is how, for a fixed number of edges, the degree distribution influences the flow of information. As the Laplacian governs the continuous-time *edge-centric* random walk, the presence of large hubs implies an enhancement of the process with faster propagation of the diffusing quantity [16, 24]. As the free energy is inversely related to the partition function, $Z = \sum_{i=1}^N e^{-\tau \lambda_i}$, the bounds of the former are given by the bounds of the latter. From $1 \leq Z \leq N$, where the lower bound is given for the connected network at large $\tau \gg 1$, while the upper bound is given by a network of isolated nodes $\forall \tau$, or for a connected one at small scales $\tau = 0$. Thus, the $-\log N/\tau \leq F \leq 0$ and the gain in information flow is reflected by the variation of the free energy from the case of isolated nodes:

$$W = \delta F = F - F_{iso} = F + \frac{\log N}{\tau} \geq 0 \quad (4)$$

which is tantamount to the work in the canonical ensemble. Moreover, $U = W + Q \geq 0$ which implies $W \geq |Q|$. A formation process can be depicted as the trade-off between these two necessities of the networked complex system: the need to maximize the information flow, while at the same time retaining an amount of structural entropy such that the network can encode and express sufficient diversity through its traits.

Thus, to complete the analogy to thermodynamics, the trade-off between the diversity of information and information flow is captured by the efficiency [1]:

$$\eta = \frac{W + Q}{W} = 1 - \frac{|Q|}{W} = \frac{U}{W} \quad (5)$$

where $0 \leq \eta \leq 1$ and $U \equiv -\partial_\tau \log Z \equiv \text{Tr}[\hat{L}\hat{\rho}]$. The variational principle here exposed has been devised to macroscopically explain the sparsity and its empirical scaling law, as well as the emergence of topological features such as modularity, small-worldness, and, with partially less clear results, heterogeneity [1]. In our work, we use this variational principle to explain the structural properties of the network subclass composed of heterogeneous hierarchical trees. An additional element is that these trees are required to encode the diversity expressed in the environment they are in contact with, defined by a real-world dataset of patterns. The specific heat is used here to identify which is the resolution scale at which such a variational principle is effective for our subclass of networks during the transition to the scale-invariant regime. For scale-invariant networks, for some τ -scales, $U = \langle \lambda \rangle_\tau = C_0/\tau$ [3, 23], hence in this regime Equation (5) becomes $\eta = \frac{1}{\tau} \frac{C_0}{W}$.

3 Methods

Our results are evaluated over subsets of four different datasets: the NIST [25], the MNIST [26], the FashionMNIST [27], and the CIFAR10 [28] datasets. These datasets contain randomly collected instances of image samples out of 10 classes. It should be noted that in this type of data, a pattern class can generally not be represented by a single centroid vector, but will contain multiple densities ('sub-style patterns') such that the sample point cloud can be ordered naturally in a network structure.

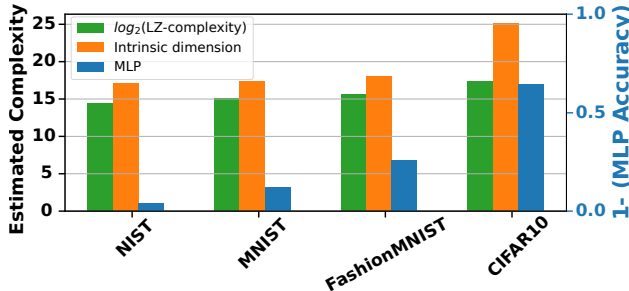


Figure 2: **Dataset complexity** is estimated with multiple methods for each training dataset of 2000 samples encountered in this work. In green an estimate is given computing the Lempel-Ziv complexity [29], while in orange the intrinsic dimension is estimated with the Maximum Likelihood Estimation approach [30, 31, 32]. In blue the accuracy on the test set for a multilayer-perceptron (MLP) with two hidden layers of 128 units each. The left axis refers to the quantities in green and orange, while the right axis refers to the multilayer-perceptron accuracy. We observe that the CIFAR10 dataset is the most complex one, while the NIST dataset is the least complex among the four.

The MNIST database contains 24×24 grey-scale images of handwritten digits [0-9] commonly used to benchmark machine- and deep-learning algorithms. The NIST dataset is the ancestor of the MNIST, it contains 16×16 black-and-white images of the handwritten digits [0-9]. The FashionMNIST is a large dataset of 28×28 grey-scale images of fashion products from 10 categories. The CIFAR-10 dataset contains 32×32 color images belonging to 10 classes. In all our experiments a subset of 2000 samples is extracted from the train set and the test set independently. Samples from the FashionMNIST and MNIST are always binarized, while the samples from the CIFAR10 are normalized between 0 and 1 dividing each pixel value by 255, and values are rounded up to eighth decimal. In the Supplementary we show also the same results for larger networks generated from 4000 samples from the MNIST and FashionMNIST. The 10 classes are equally represented both in the test and in the training set. The datasets used in our experiments exhibit different levels of complexity, see Figure 2. We estimate with multiple methods the dataset complexities on the same subset of 2000 training samples used in the rest of the manuscript. The first heuristic approach is based on the test accuracy of a small multilayer perceptron (2 layers with 128 units each). In pattern recognition, the complexity of a dataset is determined by the complexity of the curvilinear hyperplanes that would be needed to optimally separate patterns from different classes. A simple but effective parameter to gauge this facet of complexity is the accuracy that a classifier (such as the MLP) can achieve in determining the true class label for a data point. Thus, a more complex dataset would result in a lower accuracy for neural networks of fixed size when compared to a less complex dataset. The second method we use is the computation of the Lempel-Ziv complexity [29] of the aggregated training set. In this case, samples need to be binarized. The third method concerns the measure of the intrinsic dimension [15, 32] of the dataset using the Maximum Likelihood Estimation approach introduced in [30] with the correction proposed in [31]. A given dataset of gray-scale images of size $pixel \times pixel$ a priori lies on a high-dimensional space of $\mathbb{R}^{pixel \times pixel}$, nevertheless, because it might contain a specific class of objects that account for the "world" of our problem, for instance, handwritten digits, it spans a lower dimensional manifold. Even though the definition of such a manifold is an open problem, it is possible to estimate its dimension based on the distance of the n -neighbouring points [15, 32]. We set the hyper-parameter $n = 3$.

While in Section 4 we discuss the full range of r , in Section 5 we limit the discussion to $r \leq 0.85$ as the accuracy, and hence the pattern-matching efficiency, quickly drops for larger r , moreover the algorithm shows instability as it doesn't necessarily converge for $r \geq 0.9$. The Portegys algorithm we use is the extended version with $k = 5$ introduced in [13] where the distance between patterns is the Euclidean distance.

3.1 Pattern-matching efficiency

After the tree formation described in Section 1, the Portegys algorithm enters the search phase, where the best match to an unknown search pattern, S , is given using a first-best approach. The original goal of this algorithm was to restructure

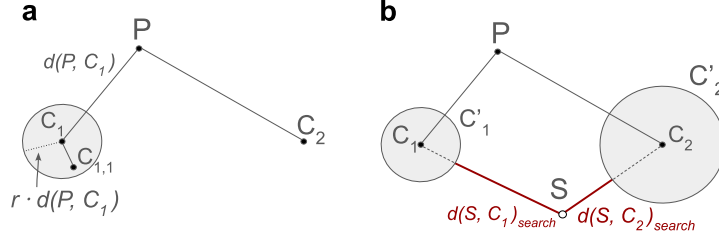


Figure 3: **Search method based on relative distance.** In (a) the growth process is illustrated. At each step, a new pattern is linked to either the current parent pattern, P , or to one of its children, C_i . The parameter r modulates the region of attraction of the child, indicated by the gray circle around C_1 , and the one of the parent node. Points falling within the distance $r \cdot d(P, C_i)$ are linked to the child, otherwise, an edge will be defined between the parent node P and the new pattern. In (b) the search method based on relative distance is illustrated. Once a search pattern arrives at node P it must choose to search either the subtree of C_1 or C_2 . The choice is based on minimizing the distance to the expected patterns contained in the subtree of C_i . In the depicted case, patterns closer to the search pattern S are expected to be in the subtree of C_2 . Adapted from [33].

a list of examples in a tree-based way, such that the matching accuracy would not be much worse than nearest-neighbor matching on a full list while providing a considerable speed up due to the hierarchical organization into a tree-based structure. The growth process, described in Section 1 and depicted in panel (a) of Figure 3, ensures that subtrees of a given node have on average decreasing distances for decreasing hierarchical levels. This provides the possibility of using a search technique based on relative distances. The search method is depicted in panel (b) of Figure 3 and is an iterative process that begins at the root-node pattern. Once a search pattern, S , arrives at a certain parent node, P , it must decide to continue to search for the best match into one of its children subtree, C'_1, C'_2 in Figure 3. The choice is taken minimizing the Portegys search-distance: $d(S, C_i)_{search} = d(S, C_1) - r \cdot d(P, C_i) = d(S, C'_i)$, which quantifies the distance between the S -pattern and the potential patterns appearing in the subtree of each child C_i , collectively indicated by the gray circle C'_i in panel (b). Where $d(\cdot)$ indicates any metric distance equipped with semi-positivity, symmetry, and triangular inequality properties. If $d(S, C_i)_{search}$ is less than zero then it is set to zero. In panel (b) the bold segments in red indicate the search distance to each child node and equivalently the expected distance between the unknown pattern S and their expected neighborhoods of patterns C'_i .

It is natural to define a pattern-matching efficiency, θ , in terms of class match accuracy, A , and the number of distances computed, N_{dist} :

$$\theta = \frac{A}{\log N_{dist}} \quad (6)$$

the logarithm is taken since the range of N_{dist} can virtually span the interval $N_{dist} \in (0, N]$, where N is the number of nodes. For the case of a star graph, $r \rightarrow 0$, the number of computed distances is maximum $N_{dist} = N$, for lower values of r the number of computed distances decreases, potentially decreasing the class-match accuracy. When defining the pattern-matching efficiency we are making the simplified assumption that the pattern-matching algorithm runs on a physical substrate such that visiting any node has a fixed cost in terms of energy or terms of general resources. Hence, the efficiency θ quantifies the trade-off between the cost of used resources and the gain in performance, as depicted in panel (c, f) of Figure 4 for the MNIST and CIFAR10 respectively. Note in panel (d) that the CIFAR10 dataset has a peak for accuracy which we interpret by saying that for complex datasets (see also the case of the FashionMNIST in Section S7) some network structures do possess the ability to better encode information of the "world" in their traits. We postpone the discussion of this finding to Sections 5 and 6.

4 Phase portrait

The Portegys algorithm produces tree structures as those depicted in panel (b) of Figure 5 depending on the value of the control parameter r . Two structural phase transitions involving two different resolution scales can be identified (see Figure 5.(a)). The transition at the largest resolution scale can be described using as an order parameter a quantity that describes the large-scale network properties: $\hat{d} = d/m$, where d is the diameter of the tree and m is the number of edges equal to $m = N - 1$. For hierarchical trees, another choice would be the normalized number of hierarchical levels $\hat{h} = h/(N - 1)$ where h is the number of hierarchical levels ranging from $h \in [0, N - 1]$ (see illustration in

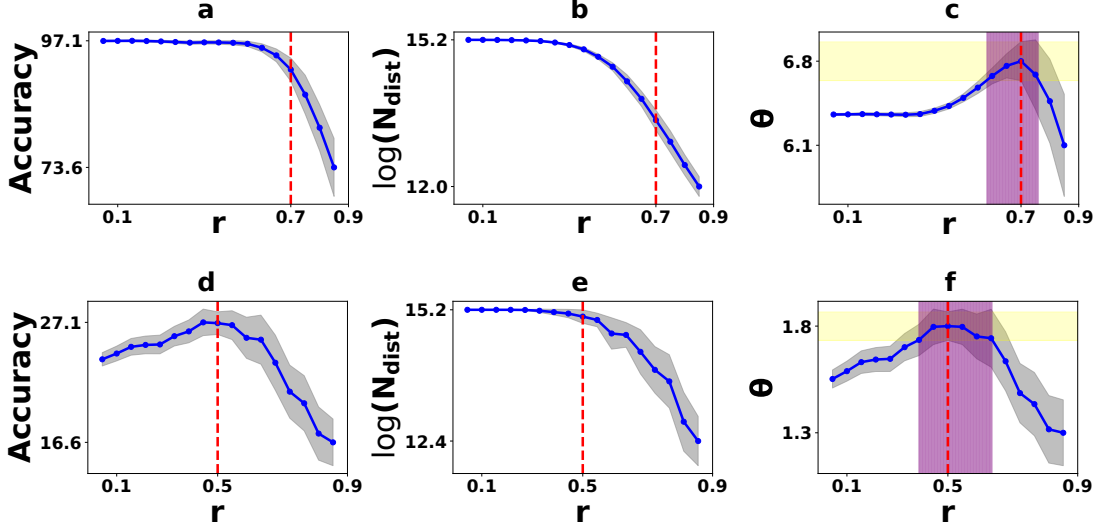


Figure 4: **Pattern-matching efficiency** in (c, f) measured over the NIST and CIFAR10 respectively. The efficiency θ is defined as the trade-off between the classification accuracy, (a, d), and the logarithm of the number of distances computed to find the best match, (b, e). The dashed-red vertical line indicates the optimal r value in terms of efficiency θ . The shaded grey area designates the standard deviation. The purple shaded area in panel (c, f) indicates a tolerance r -domain of optimal efficiency. The tolerance domain is defined as the r -values such that the corresponding θ -values are included in one standard deviation computed at the maximum θ , whose y-axis projection is indicated by the yellow shaded area. Curves are computed over 50 independent simulations with a subset of 2000 samples extracted from the NIST and CIFAR10 datasets. The 10-digit classes are equally represented both in the train- and test sets.

panel Figure 6.(b)). Both quantities describe the "volume" expansion controlled by the parameter r . We chose the normalized diameter \hat{d} and we identify this phase transition at $r \sim 1.05$ as indicated by the peak of the variance (dotted lines) in Figure 6.(b) for the two network sizes $N = 500, 1000$. This phase transition border distinguishes between networks in the amorphous regime from those with regular 1d-lattice structure. Note that before the transition point, at $r \sim 0.8$ the spectral dimension is $d_s = 4/3 = 2C_0$, typical of random trees with finite variance in the node degree's distribution [34], where C_0 is the specific heat plateau height (see also Section 4.(a, c)). For $r \gtrsim 1$, $d_s = 1$, as it is expected for a 1d-lattice.

The second change of phase is the transition from the star graph to the amorphous configuration at $r \sim 0.35$. Here, the emergence of scale-invariant structural properties is reflected by the progressively larger specific heat plateau in between the two C -peaks, as shown in (a) and (c) of Figure 5. For $r \rightarrow 2$, the plateau would include the full 1d-lattice in the thermodynamic limit $N \rightarrow \infty$.

Before the transition, a single peak in the specific heat identifies a single trivial τ -resolution scale below which the informationally connected components are the single nodes, and after which the informationally connected component is the full graph. After the phase transition, a second peak of the specific heat emerges at larger τ scales. This second peak of C in Figure 5.(c) identifies the scale at which the information is integrated between the distinct modules. In other words, the second peak reflects the "degree" of the large-scale modules, in much analogy to the first peak, which reflects the presence of hubs at the local connectivity scale of the nodes. Note that we exclude both the clusters, i.e. triangles, and higher-order cycles from our discussion as the tree networks we address are purely loop-less.

This second change of phase is the one mainly investigated in this work as the peaks in the thermodynamic and pattern-matching efficiencies always occur in the scale-invariant region of the phase plane, and in some cases, they occur in the vicinity of this transition border $r \sim 0.35$. This transition, conversely to what we did with the amorphous to regular-lattice transition discussed above, can't be identified by a quantity resolving the large-scale property of the network. Indeed, we observe in Figure 6.(b) the lack of a peak in the variance of \hat{d} , which would indicate no sign of *bona fide* phase transition. Nevertheless, a phase transition exists and an appropriate order parameter needs to be employed to identify it.

This phase change occurs at smaller resolution scales with respect to the first phase transition we discussed. Specifically, it involves the mesoscales properties changing from the star graph to the scale-invariant regime (see the bifurcation in the

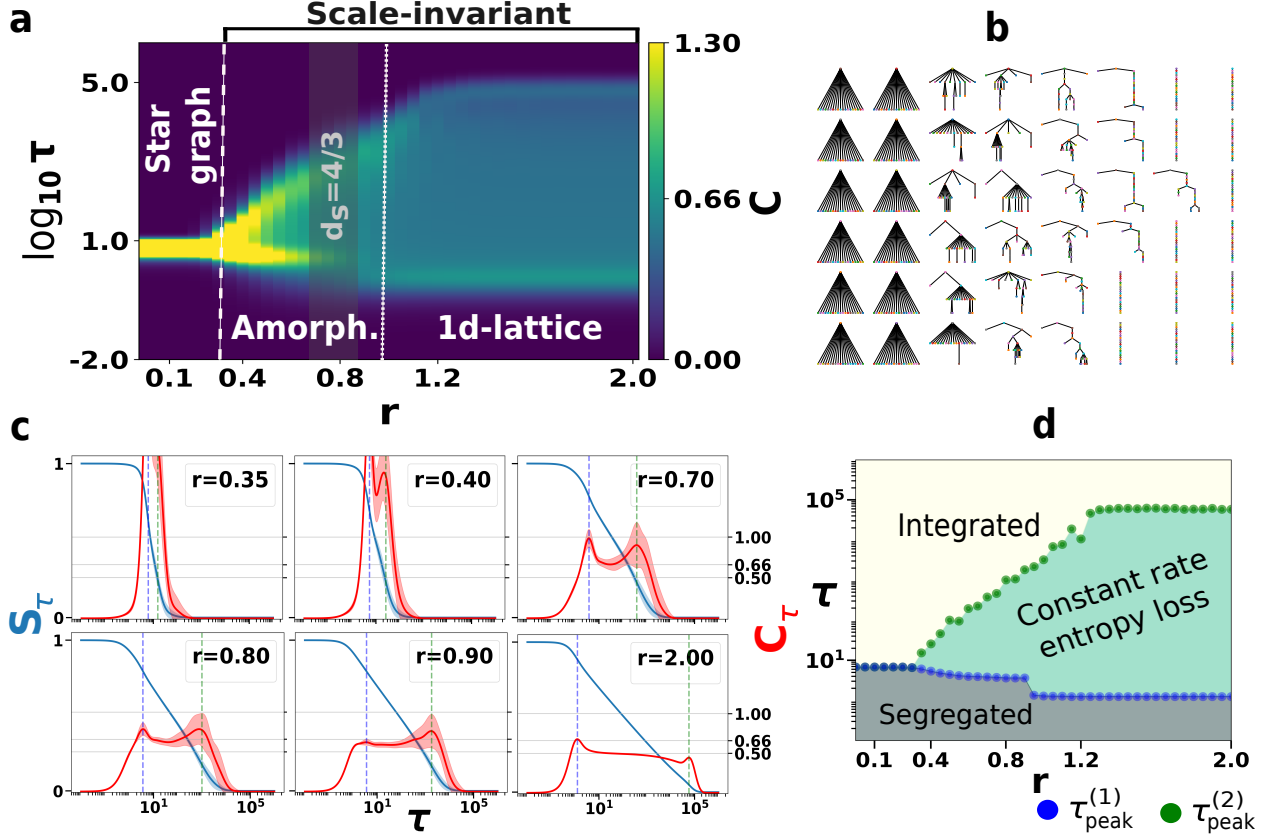


Figure 5: **Multiple phase transitions in hierarchical tree networks.** In (a) the specific heat, C , across the range $r \in [0, 2]$. At $r \sim 1.35$, indicated by the dashed white line, the hierarchical network transits from the star graph to the amorphous configuration with the emergence of scale-invariant traits evidenced by a plateau in the specific heat. The scale-invariant region shows a second phase transition from amorphous to regular 1d-lattice at $r \simeq 1.05$ indicated by the dotted white line. For $r > 0.35$, the network is always scale-invariant with decreasing spectral dimension up to the transition point, above which the spectral dimension saturates to $d_s = 1 = 2 \cdot C_0$, where C_0 is the plateau height in (c). Note that at $r \sim 0.8$ the spectral dimension is $d_s = 4/3$ as expected for random trees with finite variance in the node degree. In panel (c) the entropy (blue) and the specific heat (red) for $r = \{0.35, 0.40, 0.70, 0.80, 0.90, 2.00\}$. Vertical blue and green lines indicate the τ -scale of the first and the second peak, $\tau_{peak}^{(1,2)}$, of the specific heat respectively. In (d), the τ -scales of the two specific heat peaks are illustrated with blue and green dots respectively delimiting the three dynamical phases: the segregated phase (grey), the integrated phase (light yellow) and the green region where *self-similar structures* are integrated at a constant-rate. In (b) exemplary hierarchical trees of $N = 20$ for growing r from left to right. All curves in this figure are realized for networks of $N = 500$ randomly sampled from the FashionMNIST dataset and averaged over 50 independent realizations.

specific heat in Figure 5.(a),(c)). Thus, we can identify this transition using as an order parameter the modularity [35], Q , of the tree which we show in panel (a) of Figure 6. We are taking advantage of the fact that the modularity for trees is bounded between $[0, 1]$ and that in the case of a 1d-lattice, the modularity is equal to 1 if we partition the network into N communities, which is the case if we use the community detection algorithm introduced in [36]. We stress that modularity is a mesoscale descriptor while the diameter of the network is a large-scale descriptor. This motivates the choice of a mesoscale $\tau \sim 10$ employed in Section 5 that can resolve structural changes from the star graph phase to the amorphous scale-invariant phase.

As a second possible order parameter, for the mesoscale phase-transition, we show in Figure 6.(c) the difference of entropy at the two $\tau_{peak}^{(1,2)}$ peaks. This order parameter counts the normalized (log)number of informationally connected nodes across the τ -scales of the specific heat plateau. In simple terms, we count the fraction of nodes included in the scale-invariant region. We observe a discontinuity at the border of the scale-invariant transition that is not observed at the border of the amorphous to regular lattice transition.

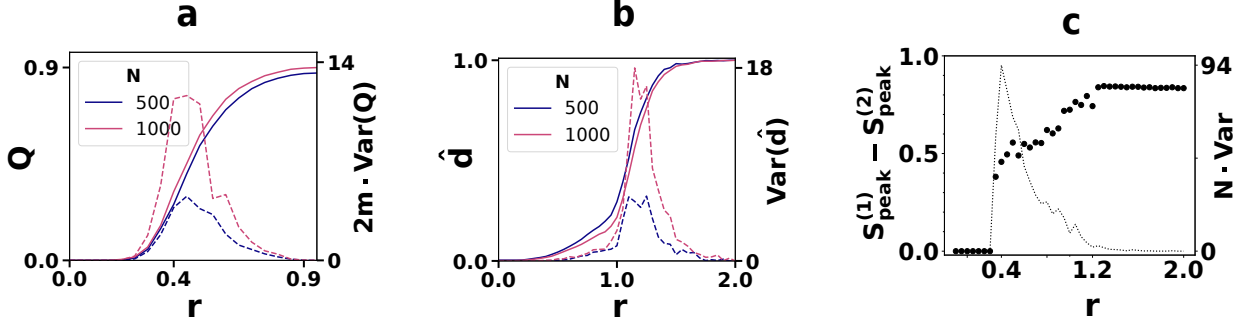


Figure 6: **Order parameters.** In (a), the modularity, Q , resolves the transition involving the mesoscale structure. In (b), the normalized diameter, $\hat{d} = d/m$ resolves the large-scale transition. Their respective variances (dashed lines) identify the transition points. In (c), the difference of entropy at the two $\tau_{\text{peak}}^{(1,2)}$ peaks quantifies the normalized (log)number of informationally connected nodes across the scale-invariant τ -domain, i.e. the number of nodes included in the scale-invariant region. Note the discontinuity at the transition from star to amorphous. Curves in (a-b) are realized for networks of $N = 500, 1000$ randomly sampled from the FashionMNIST dataset and averaged over 50 independent realizations if not specified elsewhere. Curves in (c) are for networks of $N = 500$.

As already discussed in Section 2.1, also along the τ -direction a phase transition exists [22, 3] delimited by the two peaks of C in $\tau_{\text{peak}}^{(1,2)}$ and, in between the two, we can distinguish three *dynamical* phases (see Figure 5.(d)). For $\tau < \tau_{\text{peak}}^{(1)}$, the network is in the informationally segregated phase; while for $\tau > \tau_{\text{peak}}^{(2)}$ is in the informationally integrated phase. Only for $r > 0.35$ and $\tau_{\text{peak}}^{(1)} < \tau < \tau_{\text{peak}}^{(2)}$, we observe the *dynamical* regime of *constant-rate entropy loss* characteristic of scale-invariant structures with dilation symmetry [3, 23].

5 Results

Figure 7 shows the pattern-matching efficiency defined in Equation (6) and the thermodynamic efficiency of Equation (5) for the four investigated datasets.

Panels (a)-(d) depict the thermodynamic efficiency, η , and panels (e)-(h) depict the pattern-matching efficiency, θ . The vertical dashed lines indicate the peaks of the efficiencies, while the shaded purple regions in (e)-(h) indicate a r -domain tolerance for θ . The tolerance domain is defined as those r -values such that the corresponding θ -values are included in one standard deviation computed at the best trade-off.

Note the consistency in the global maxima of θ and η in terms of optimal r for the NIST and the FashionMNIST. See the r -range spanned by the purple-shaded areas in panels (e)-(h) and the vertical dashed lines in panels (a)-(d). This consistency in the maxima suggests that the two efficiencies might be related, for the specific context of this algorithm. In the Section 6 we discuss this matter.

The topological complexity of the networks increases at a critical r from the trivial traits of a star graph to the fractal structure of the amorphous network. Thus, the emergence of structure is reflected by the rise of a second peak in C together with a roughly $C = C_0 > 0$ plateau in between the first and the last peak as is illustrated in panels (i)-(l) for the investigated dataset. Such transition is also depicted in Figure 8 by the bifurcation of the blue and green curves for $\tau_{\text{peak}}^{(1)}$ and $\tau_{\text{peak}}^{(2)}$ indicating the lower and upper branches in panels (i)-(l) of Figure 7. See also Section S4 which illustrates the spectral entropy and specific heat curves for the four datasets independently depicted for each r -value.

We note that the specific heat of the MNIST has a third large peak in between $\tau^{(1)}$ and $\tau^{(2)}$ (see panel (k) in Figure 7). This is an intrinsic characteristic of the dataset, as it is only mitigated for larger networks, as shown in Section S2 of the Supplementary. This intermediate peak is sufficiently strong to be reflected on a local maximum of η , in Figure 7.(c). Although this local maximum in η is not detected by θ in Figure 7.(g), it is reflected in its standard deviation, allowing us to include the r -range indicated by the shaded purple area when we compare η and θ peaks in terms of r . This shaded region corresponds to the η -peak-to-peak r -range in Figure 7.(c).

Remarkably, the thermodynamic efficiency is computed at the specific resolution scale $\tau \sim 10$ involved in the mesoscale structural transition from star graph to amorphous scale-invariant discussed in Section 4 and fig. 6. Such critical

resolution scale is identified by the bifurcation of the specific heat peaks in panels (i)-(l) of Figure 7 and in panels (a)-(d) of Figure 8. In the seminal work [1], it is suggested to compute the thermodynamic efficiency, η , using as a reference the τ -scale equal to the inverse of the Fiedler eigenvalue, i.e. the smallest non-zero Laplacian eigenvalue $\lambda_2 = 1/\tau_{diff}$, and logarithmically divide τ_{diff} to define the large propagation scales, the middle scales, and the small scales. In fact, this eigenvalue should provide the time scale where the diffusion process has reached equilibrium.

Nevertheless, on the one hand, τ_{diff} only approximates the end of the diffusion process which is better reflected by $\tau_{peak}^{(2)}$. Panels (a)-(d) of Figure 8 depict the τ_{diff} in red next to the $\tau_{peak}^{(1,2)}$ curves. The key difference is in the use of the thermal ensemble average which employs all the eigenvalues to compute the specific heat.

It is crucial to identify the τ -scale that resolves the phase transition from the single trivial scale of the star graph to the more complex topological traits of the amorphous network depicted in Figure 5.(b). We consider such resolution scale of significant importance for the computation of the efficiency η across the transition as it defines an "ultra-violet" cut-off in the characteristic frequency of the network across the transformation, similarly to what was discussed in the context of the Laplacian-Renormalization group [3]. In Section S3 of the Supplementary Material the efficiency, η , is computed in the range interval $\tau < 10$ as is indicated by the diffusion time defined in [1] $\tau_{diff} = 1/\lambda_2$, i.e. the red curves depicted in panels (a). Whether computed at those scales, η shows a change in concavity and no relation with the pattern-matching accuracy.

Finally, note in Figure 8 the slow down of diffusion due to the increasing "volume" of the network discussed in Section 4 and indicated by the $\tau_{peak}^{(2)}$ curve as a function of r . We remark that $\tau_{peak}^{(2)}$ is a function of the parameter r only, and the latter shapes the degree distribution only, as the number of nodes and edges is fixed across the transition. We note that the Portegy's algorithm stays in the regime of sparsity, symbolically $\delta(\frac{N-1}{|E|} - 1)$.

5.1 Performance at the emergence of scale-invariance

In this section, we discuss the relation between the location of the pattern matching efficiency, θ , on the phase plane of the algorithm and the complexity of the dataset, see Figure 2. We turn our attention to the panels (e)-(h) and (i)-(l) in Figure 7 and panels (a)-(d) in Figure 8.

For the CIFAR10 and FashionMNIST datasets, there is a rough correspondence between the r -value where the structural transition emerges, $r \sim 0.5$ for CIFAR10 and $r \sim 0.35$ for FashionMNIST, and the r -range where the peaks of each of the two θ efficiencies are observed, $r \in (0.30, 0.50)$ and $r \in (0.35, 0.55)$ respectively. Note that for the FashionMNIST, also the thermodynamic η peaks in the same range of r .

On the other hand, for the MNIST and NIST datasets, θ peaks in ranges of r which are farther away from the respective bifurcation points $r \sim 0.4$ and $r \sim 0.5$. The term "far away" is quantified by the purple-shaded areas in panels (e)-(h) of Figure 7. Note the correspondence of the peaks of η and θ for the two datasets in terms of r . The latter observation on the correspondence of θ and η also holds for the MNIST, if we include θ points in the one standard deviation illustrated by the shaded-purple area.

To explain the varying locations of peak efficiencies, whether near the transition border or farther from it, we refer to an argument in the literature [37, 10, 38]. A system needs tuning, or self-tuning, at the edge of a phase transition only when the task demands a high level of complexity, specifically, this was investigated in the context of second-order phase transitions [37, 10].

For the more complex datasets CIFAR10 and FashionMNIST, the optimal θ values are closer to the transition border. In contrast, the optimal values for the simpler NIST and MNIST datasets are located farther from their respective transition points. This observation also holds for the thermodynamic η for the FashionMNIST, MNIST, and NIST. Moreover, the MNIST, an intermediate dataset in terms of complexity, is an interesting case. It shows two maxima for the thermodynamic efficiency, η . The global maximum in Figure 7(c) is far away from the critical value of r illustrated by the bifurcation in panel (c) of Figure 8, while the local maximum is at $r \sim 0.35 - 0.40$, which corresponds to the critical value of r indicated by the bifurcation.

These observations align with the hypothesis that the system exploits its proximity to the phase transition boundary only when presented with a relatively complex task. The overall discussion highlights the importance of the dataset under analysis, particularly its disordered distribution of points within a high-dimensional feature space.

Finally, we observe that while the value of r where a structural transition appears is dependent on the dataset, i.e. $r = 0.50$ for the NIST, $r = 0.40$ for the MNIST, $r = 0.35$ for the FashionMNIST and $r = 0.50$ for the CIFAR10, the $\tau \sim 10^1$ scale is roughly the same for all the four datasets. Interestingly, the bifurcation τ -scale is also unaffected by the number of nodes in the network (see Supplementary Section S2). We speculate about the possibility that this is due to the constraint on sparsity as it is an invariant feature over the cases investigated in this work.

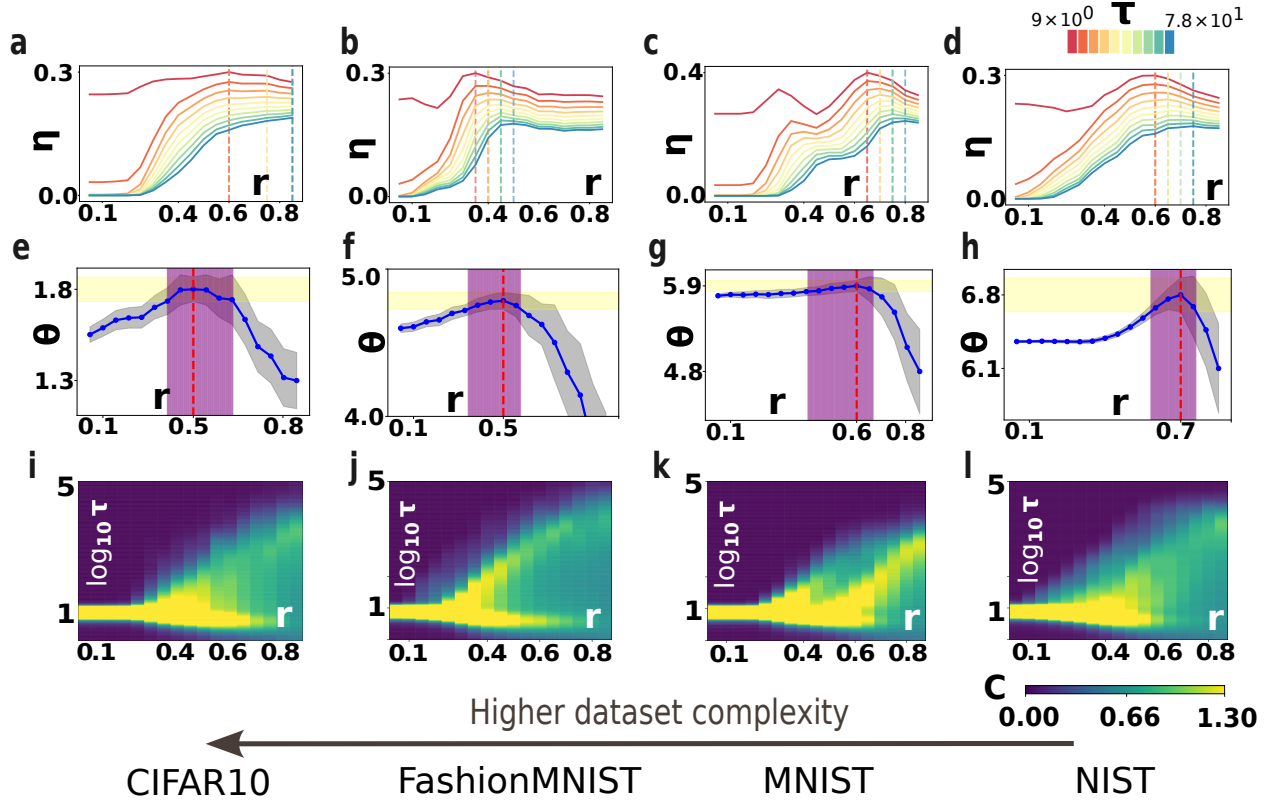


Figure 7: **Thermodynamic & pattern-matching efficiency.** In (a)-(d) the thermodynamic efficiency, η , as a function of r . The thermodynamic efficiency is measured in the τ -range of one order of magnitude from the bifurcation of the specific heat, C , depicted in panels (i)-(l). The τ -resolution scale $\tau \sim 10$ identifies the relevant "length" scale resolving the transition from the single-peak to the emergence of a roughly plateau region, $C = C_0 > 0$, reflecting a roughly scale-invariant structure. In (e)-(h) the pattern-matching efficiency, θ , is plotted as a function of r for the four investigated datasets of increasing complexity (see arrow at the bottom of the figure). The shaded purple area indicates the tolerance r -range for the optimal pattern-matching efficiency, which includes points in one standard deviation from the global maximum indicated by the vertical red-dashed line. In panels (b)-(f) and (d)-(h) a noticeable cohesion of the peaks of the two efficiencies is observed. Vertical dashed lines indicate the global maxima of the efficiencies. The efficiency peaks, both η and θ , are always in the amorphous region of the phase plane. For datasets of higher complexity, they tend to be closer to the structural phase transition border separating the star-graph to the amorphous region. This agrees with the argument that a fairly simple dataset does not benefit from the vicinity of the phase transition. Quantities are averaged over 50 independent simulations.

6 Discussion

The ability of a system to survive is the capability of concentrating a flow of order from the environment - "drinking order from the environment" [39]. In other words, systems, whether living systems or machine(-learning) systems, need to learn an efficient internal representation of the complex world - or the dataset - they are posed in contact with. Such internal representation can be encoded in terms of abstract probability distributions [9, 10] or into the very network features of the system, as it happens in genetic regulatory networks playing a central role in morphogenesis [40], or in a mixed way as in artificial neural networks where the engineer designs a complicated distribution through the definition of the architecture and the training phase fills in the parameters to obtain the desired function-approximation machine to achieve statistical generalization [41].

When confronted with the real-world environment, to survive, living systems not only need the capability of interpreting the environment, but they also need the capability to quickly react with a coherent response to stimuli possibly drawn from the same distribution they adapted to [42]. Moreover, the same system needs to cope with the cost of sending information across its structure which can cause an enhanced exploitation of resources. In the context of machine

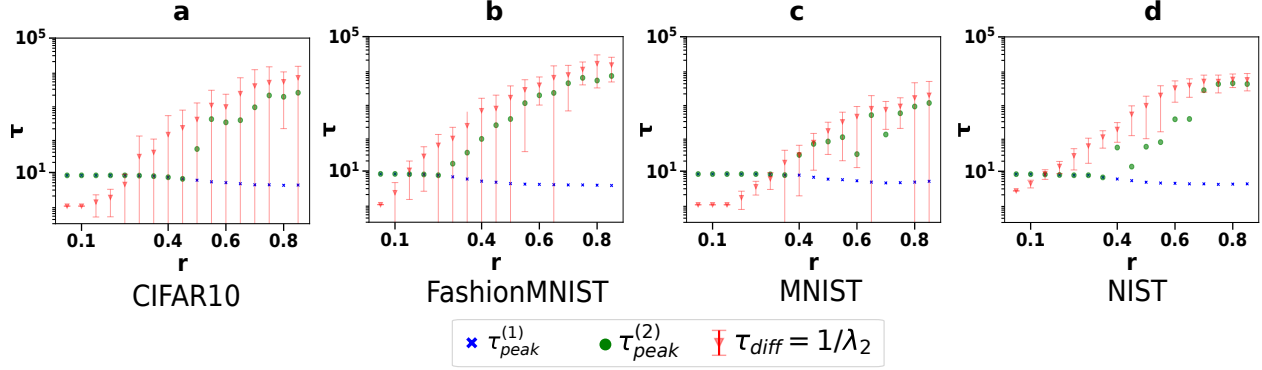


Figure 8: **Role of the ensemble average on the estimation of the τ -scale.** Panels (a)-(d) depict the $\tau_{peak}^{(1,2)}$ and τ_{diff} as a function of r . $\tau_{peak}^{(1,2)}$ are the τ -location of the first and last peak of the specific heat in Figure 7. τ_{diff} is the inverse of the Fiedler eigenvalue which provides a good estimation of the end of the diffusion process only for sufficiently large r . Note that the red curves retrace the profile of the upper branch of the specific heat for $\tau \gtrsim 10$ in panels (i)-(l) of Figure 7. At smaller r values the equilibrium time is better reflected by $\tau_{peak}^{(2)}$. The equilibrium of the diffusion process is an increasing function of r . τ_{diff} curves are averaged over 50 independent simulations. The $\tau_{peak}^{(1,2)}$ curves are computed from the specific heat curves which are averaged over 50 independent simulations.

learning, the cost can be quantified by the number of computations to be done before the satisfying answer to the task can be reported, e.g. class-matching.

The recently developed theoretical tools of statistical physics for networks [5, 4, 43, 22, 3, 1] permit to quantify the diversity in the traits of the network, with the von Neumann entropy, and the transmission flow of information, with the Helmholtz free energy. As fastness of information flow and sufficiently rich representation of the external world are two competing capabilities, the formation process of a complex networked structure can be interpreted as the macroscopic thermodynamic outcome of the delicate balance between the two, and a variational principle in terms of thermodynamic efficiency can be devised to explain why a certain structure emerge in place of an other [1].

In our work, this variational principle is computationally employed to explain the structural properties of the network subclass composed of sparse heterogeneous hierarchical trees produced by the Portegys protocol that, similar to living systems, need to learn the diversity of the environment they are in contact with and consequently self-organize their structure. The tree formation undergoes two phase transitions at two different scales: the former is a mesoscale transition with the emergence of an approximately scale-invariant structural behavior progressively involving larger scales; the latter is a large-scale transition from the irregular scale-invariant structure to the regular-scale invariant 1d lattice.

Given that the original purpose of the algorithm was an efficient pattern-searching method, we have investigated the pattern-matching efficiency and its positioning on the phase-plane for four different datasets with different levels of complexity. The optimal pattern-matching efficiency was always found in the amorphous regime, Nevertheless, when the dataset was more difficult, an optimal efficiency to the pattern-searching task was found close to the transition border separating the star-graph and the scale-invariant regimes.

Moreover, empirical evidence suggests that the thermodynamic efficiency and the pattern-matching efficiency show some consistency, namely when we look at the global maxima of the two in the r -range. Even though the two processes involved possess significant differences, namely the Portegys search phase is a directed process starting from the root node, while the diffusion propagator describes an ergodic process propagating from any possible node, we think that is reasonable to expect some similar behavior of the two efficiencies, as both quantities, in the end, estimate a trade-off between the flow of a process and the encoding capabilities of the system in its network structural traits when confronted to the disorder embedded in a dataset of real-world patterns.

In both cases, the "flow" is quantified by a monotonic decreasing quantity as a function of r . For the Portegys we have the logarithmic number of computed distances, while for the Laplacian process, we have $\delta F = F + \frac{\log N}{\tau}$, where $F = -\frac{\log Z}{\tau}$. It is easy to convince ourselves that these two quantities describe the flow in the network as the former counts the number of visited nodes across the traversing of the network by the Portegys search process, while the latter is minus the logarithm of Z , with Z proportional to the average return probability after time τ of a continuous time

edge-centric random walker [4]. They are not exactly alike as only the latter is an ergodic process; still, they can be used as estimates of the "flow".

We have discussed the denominator of the two efficiencies: η and θ . We now discuss the numerator. For what concerns the Portegys algorithm, we have observed that there are more descriptive network structures *per se* as evidenced by the fact that the accuracy is not necessarily a monotonic decreasing function of the control parameter r , but it can exhibit higher values at specific r -values as illustrated by the cases of the CIFAR10 and the FashionMNIST.

The matter is what makes a certain structure better suited in terms of accuracy to a given task, or equivalently in terms of a complex input-output mapping. Analogously to artificial neural networks, enlarging the number of parameters eventually results in achieving more complicated functions, even though this doesn't imply a one-to-one relation between the two. In the case of a network structure, the parameters are the network traits themselves, which in the Fourier space become the "network frequencies", λ_i , i.e. the Laplacian eigenvalues. We can measure an effective number of parameters by computing the thermal average of the frequencies contained in the network, precisely the numerator in Equation (5). The internal energy, U , is the Gibbs average of the Laplacian eigenvalues of the network at the operational resolution scale, τ , tantamount to the inverse temperature, β , in statistical physics. Thus, the Gibbs average frequency content is quantified by the internal energy, $U_\tau = \text{Tr}[\hat{\rho}\hat{L}] = \langle \lambda \rangle_\tau$, where for scale-invariant networks $\langle \lambda \rangle_\tau = C_0/\tau$ [3]. The difference to the case of the artificial neural network is that we can't directly increase the number of parameters, given a fixed number of samples, but we can let the structure self-organize given the value of the external control parameter, r .

Notably, we have computed the thermodynamic efficiency at a specific resolution scale, τ . We have used the specific heat $C = -dS/d\log\tau$ to identify the τ -resolution which resolves the transition from the trivial structure, that is a single specific heat peak, to the emergence of more complex structures, where the specific heat shows some plateau reflecting the growth of a scale-invariant region where information is integrated at a constant rate. Such τ -resolution scale is akin to an "ultra-violet" cut-off delimiting the relevant frequencies of the network structure across the transition to scale-invariance, i.e. from star graph to amorphous. The operational τ -scale employed roughly identifies the scale where modules emerge in the network. For this reason, we could gauge the phase transition employing the network modularity, Q , as an order parameter. While the transition to scale-invariant permits the identification of the network resolution scale, τ , where the thermodynamic efficiency needs to be measured to observe a peak, the corresponding transition value of the control parameter, r , does not always coincide with the global maximum in the efficiency. We explain this with the statement that a system benefits from the vicinity to a phase transition only when it confronts environments of higher complexity, while it does not benefit from it when the environmental complexity is lower. This is elucidated by the use of four different datasets of increasing complexity and supported by other works in the literature [37, 10, 38].

In terms of practical utility, the methods presented could in principle provide diagnostics to tree-based approaches to classification such as hierarchical clustering, even though a limitation of this study is the investigation of only the Portegys algorithm. Given a pre-trained tree network based upon an unknown dataset, it might be possible to qualitatively identify the complexity of the dataset and the ability of the tree structure to cope with that complexity based on the position of the peaks of the pattern-matching and thermodynamic efficiency on the phase plane without performing any test phase. As discussed in this manuscript, if the trained network is "struggling" in the representation of the dataset, the peak of the pattern-matching efficiency might be at the phase transition boundary providing higher accuracy at the cost of a slower pattern search. Interestingly, our analysis of hierarchical tree networks could be applied, if further developed, to other topics in artificial intelligence. We find it particularly suited to the context of dendritic learning [44], where input units are connected to output units via loop-less paths, to guide the design of the tree-like dendritic structures for biologically inspired computing. In the context of pure neuroscience, it would also be interesting to design experiments where the dendritic structure is related to the capability of the neuron to deal with complicated input-output mapping of signals. Moreover, potential applications include the topic of neuromorphic computing [45, 46, 47] currently looking for a possible solution to the ever-increasing computational power demand of recent years. In the neuromorphic paradigm, computing devices are designed such that computation and memory are colocalized on the physical substrate in the attempt to emulate the brain learning capabilities *in materio*. The full potential of biological neural systems is likely achieved because of the interplay between their complex topological structures and the functional dynamics of a very large number of elements evolving on it [48]. Tree-like structures are currently physically implemented in materio. We mention tree structures produced at the critical point of a percolation transition [49, 50] or the electrochemically formed dendrite morphology at the origin of the resistive-switching of some memristive devices [49, 51], but also fractal trees produced in the dielectric breakdown [52], thus, their capabilities could be investigated and enhanced based on this work and future developments.

Conflict of Interest Statement

The authors declare that the research was conducted in the absence of any commercial or financial relationships that could be construed as a potential conflict of interest.

Author Contributions

DC: Theoretical framework, Conceptualization, Methodology, Simulations, Data curation, Software, Writing – original draft, Writing – review & editing. LS: Writing – review & editing, Conceptualization, Supervision, Funding acquisition.

Funding

This work was funded by EUs Horizon 2020, from the MSCA-ITN-2019 Innovative Training Networks program "Materials for Neuromorphic Circuits" (MANIC) under the grant agreement No. 861153, as well as by the financial support of the CogniGron research center and the Ubbo Emmius Funds (Univ. of Groningen).

Acknowledgments

We are thankful to Jos van Goor for providing some of the scripts that enabled efficient grid search across parameters and to Federico Balducci for the useful discussions.

Supplemental Data

The Supplementary Material includes figures referenced in the main text but omitted for clarity.

Data Availability Statement

The original contributions presented in the study are included in the article/supplementary material, further inquiries can be directed to the corresponding author/s. Datasets and scripts can be found at https://github.com/CipolliniDavide/Laplacian_Trees.

References

- [1] Arsham Ghavasieh and Manlio De Domenico. Diversity of information pathways drives sparsity in real-world networks. *Nature Physics*, 20(3):512–519, January 2024.
- [2] Eörs Szathmáry and John Maynard Smith. The major evolutionary transitions. *Nature*, 374(6519):227–232, March 1995.
- [3] Pablo Villegas, Tommaso Gili, Guido Caldarelli, and Andrea Gabrielli. Laplacian renormalization group for heterogeneous networks. *Nature Physics*, 2023.
- [4] Arsham Ghavasieh, Carlo Nicolini, and Manlio De Domenico. Statistical physics of complex information dynamics. *Phys. Rev. E*, 102:052304, 2020.
- [5] Manlio De Domenico and Jacob Biamonte. Spectral entropies as information-theoretic tools for complex network comparison. *Physical Review X*, 6(4), 2016.
- [6] Manlio De Domenico. Exploring evolution (in life) through information. <https://substack.com/home/post/p-143130785?source=queue>, April 2024. Accessed: 2024-04-16.
- [7] Chris G. Langton. Computation at the edge of chaos: Phase transitions and emergent computation. *Physica D: Nonlinear Phenomena*, 42(1–3):12–37, June 1990.
- [8] Nils Bertschinger and Thomas Natschläger. Real-time computation at the edge of chaos in recurrent neural networks. *Neural Computation*, 16(7):1413–1436, July 2004.
- [9] Iacopo Mastromatteo and Matteo Marsili. On the criticality of inferred models. *Journal of Statistical Mechanics: Theory and Experiment*, 2011(10):P10012, October 2011.

- [10] Jorge Hidalgo, Jacopo Grilli, Samir Suweis, Miguel A. Muñoz, Jayanth R. Banavar, and Amos Maritan. Information-based fitness and the emergence of criticality in living systems. *Proceedings of the National Academy of Sciences*, 111(28):10095–10100, June 2014.
- [11] Bryan C. Daniels, Hyunju Kim, Douglas Moore, Siyu Zhou, Harrison B. Smith, Bradley Karas, Stuart A. Kauffman, and Sara I. Walker. Criticality distinguishes the ensemble of biological regulatory networks. *Physical Review Letters*, 121(13), September 2018.
- [12] T.E. Portegys. A search technique for pattern recognition using relative distances. *IEEE Transactions on Pattern Analysis and Machine Intelligence*, 17(9):910–914, 1995.
- [13] Mangalagiu D. *Accélération de l’algorithme des k plus proches voisins par réorganisation arborescente de la base de données*. PhD thesis, Ecole Polytechnique, Paris, 1999.
- [14] François Jacob. Evolution and tinkering. *Science*, 196(4295):1161–1166, June 1977.
- [15] Marc Mézard. Spin glass theory and its new challenge: structured disorder. *Indian Journal of Physics*, pages 1–12, 2023.
- [16] Naoki Masuda, Mason A. Porter, and Renaud Lambiotte. Random walks and diffusion on networks. *Physics Reports*, 716-717:1–58, 2017.
- [17] William N. Anderson and Thomas D. Morley. Eigenvalues of the laplacian of a graph. *Linear and Multilinear Algebra*, 18(2):141–145, 1985.
- [18] Ernesto Estrada. *The Structure of Complex Networks: Theory and Applications*. Oxford University Press, Inc., USA, 2011.
- [19] Mehran Kardar. *Statistical Physics of Fields*. Cambridge University Press, June 2007.
- [20] Richard P. Feynman. *Statistical Mechanics: A Set Of Lectures*. CRC Press, 1998.
- [21] Paolo Moretti and Michael Zaiser. Network analysis predicts failure of materials and structures. *Proceedings of the National Academy of Sciences*, 116(34):16666–16668, August 2019.
- [22] Pablo Villegas, Andrea Gabrielli, Francesca Santucci, Guido Caldarelli, and Tommaso Gili. Laplacian paths in complex networks: Information core emerges from entropic transitions. *Physical Review Research*, 4(3), 2022.
- [23] Anna Poggialini, Pablo Villegas, Miguel A Muñoz, and Andrea Gabrielli. Networks with many structural scales: a renormalization group perspective. *arXiv preprint arXiv:2406.19104*, 2024.
- [24] Chittaranjan Hens, Uzi Harush, Simi Haber, Reuven Cohen, and Baruch Barzel. Spatiotemporal signal propagation in complex networks. *Nature Physics*, 15(4):403–412, January 2019.
- [25] PJ Grother. Nist special database 19: Handprinted forms and characters database, 1995. *National Institute of Standards and Technology*, 1995.
- [26] Li Deng. The mnist database of handwritten digit images for machine learning research. *IEEE Signal Processing Magazine*, 29(6):141–142, 2012.
- [27] Han Xiao, Kashif Rasul, and Roland Vollgraf. Fashion-mnist: a novel image dataset for benchmarking machine learning algorithms, 2017.
- [28] Alex Krizhevsky, Vinod Nair, and Geoffrey Hinton. Cifar-10 (canadian institute for advanced research). URL <http://www.cs.toronto.edu/kriz/cifar.html>, 5(4):1, 2010.
- [29] Abraham Lempel and Jacob Ziv. On the complexity of finite sequences. *IEEE Trans. Inf. Theory*, 22:75–81, 1976.
- [30] Elizaveta Levina and Peter Bickel. Maximum likelihood estimation of intrinsic dimension. *Advances in neural information processing systems*, 17, 2004.
- [31] David J.C. MacKay and Zoubin Ghahramani. Comments on "Maximum Likelihood Estimation of Intrinsic Dimension" by E. Levina and P. Bickel — inference.org.uk. <http://www.inference.org.uk/mackay/dimension/>, 2005. [Accessed 10-07-2024].
- [32] Phillip Pope, Chen Zhu, Ahmed Abdelkader, Micah Goldblum, and Tom Goldstein. The intrinsic dimension of images and its impact on learning. *arXiv preprint arXiv:2104.08894*, 2021.
- [33] L Schomaker and L Vuurpijl. *7th international workshop on frontiers in handwriting recognition: September 11-13, 2000, Amsterdam, the Netherlands : Proceedings*. International Unipen Foundation, 2000.
- [34] Claudio Destri and Luca Donetti. The spectral dimension of random trees. *Journal of Physics A: Mathematical and General*, 35(45):9499–9515, October 2002.
- [35] M. E. J. Newman. Modularity and community structure in networks. *Proceedings of the National Academy of Sciences*, 103(23):8577–8582, June 2006.

- [36] Vincent D Blondel, Jean-Loup Guillaume, Renaud Lambiotte, and Etienne Lefebvre. Fast unfolding of communities in large networks. *Journal of Statistical Mechanics: Theory and Experiment*, 2008(10):P10008, October 2008.
- [37] Benjamin Cramer, David Stöckel, Markus Kreft, Michael Wibral, Johannes Schemmel, Karlheinz Meier, and Viola Priesemann. Control of criticality and computation in spiking neuromorphic networks with plasticity. *Nature Communications*, 11(1), June 2020.
- [38] Alireza Goudarzi, Christof Teuscher, Natali Gulbahce, and Thimo Rohlf. Emergent criticality through adaptive information processing in boolean networks. *Physical Review Letters*, 108(12), March 2012.
- [39] Erwin Schrodinger and Roger Penrose. *What is Life?: With Mind and Matter and Autobiographical Sketches*. Cambridge University Press, March 2012.
- [40] Dmitry Krotov, Julien O. Dubuis, Thomas Gregor, and William Bialek. Morphogenesis at criticality. *Proceedings of the National Academy of Sciences*, 111(10):3683–3688, February 2014.
- [41] Yoshua Bengio. *Deep Learning*. Adaptive Computation and Machine Learning series. MIT Press, London, England, November 2016.
- [42] Raviv Pryluk, Yoav Kfir, Hagar Gelbard-Sagiv, Itzhak Fried, and Rony Paz. A tradeoff in the neural code across regions and species. *Cell*, 176(3):597–609, 2019.
- [43] Arsham Ghavasieh and Manlio De Domenico. Generalized network density matrices for analysis of multiscale functional diversity. *Phys. Rev. E*, 107:044304, 2023.
- [44] Shiri Hodassman, Roni Vardi, Yael Tugendhaft, Amir Goldental, and Ido Kanter. Efficient dendritic learning as an alternative to synaptic plasticity hypothesis. *Scientific Reports*, 12(1), April 2022.
- [45] Carver Mead. How we created neuromorphic engineering. *Nature Electronics*, 3(7):434–435, 2020.
- [46] Giacomo Indiveri, Bernabé Linares-Barranco, Robert Legenstein, George Deligeorgis, and Themistoklis Prodromakis. Integration of nanoscale memristor synapses in neuromorphic computing architectures. *Nanotechnology*, 24(38):384010, 2013.
- [47] Dennis V Christensen, Regina Dittmann, Bernabe Linares-Barranco, Abu Sebastian, Manuel Le Gallo, Andrea Redaelli, Stefan Slesazeck, Thomas Mikolajick, Sabina Spiga, Stephan Menzel, Iliia Valov, Gianluca Milano, Carlo Ricciardi, Shi-Jun Liang, Feng Miao, Mario Lanza, Tyler J Quill, Scott T Keene, Alberto Salleo, Julie Grollier, Danijela Marković, Alice Mizrahi, Peng Yao, J Joshua Yang, Giacomo Indiveri, John Paul Strachan, Suman Datta, Elisa Vianello, Alexandre Valentian, Johannes Feldmann, Xuan Li, Wolfram H P Pernice, Harish Bhaskaran, Steve Furber, Emre Neftci, Franz Scherr, Wolfgang Maass, Srikanth Ramaswamy, Jonathan Tapson, Priyadarshini Panda, Youngeun Kim, Gouhei Tanaka, Simon Thorpe, Chiara Bartolozzi, Thomas A Cleland, Christoph Posch, ShihChii Liu, Gabriella Panuccio, Mufti Mahmud, Arnab Neelim Mazumder, Morteza Hosseini, Tinoosh Mohsenin, Elisa Donati, Silvia Tolu, Roberto Galeazzi, Martin Ejsing Christensen, Sune Holm, Daniele Ielmini, and N Pryds. 2022 roadmap on neuromorphic computing and engineering. *Neuromorphic Computing and Engineering*, 2(2):022501, 2022.
- [48] Laura E. Suárez, Blake A. Richards, Guillaume Lajoie, and Bratislav Misic. Learning function from structure in neuromorphic networks. *Nature Machine Intelligence*, 3(9):771–786, 2021.
- [49] Jae Sung Lee, Shinbuhm Lee, and Tae Won Noh. Resistive switching phenomena: A review of statistical physics approaches. *Applied Physics Reviews*, 2(3), August 2015.
- [50] J. B. Mallinson, S. Shirai, S. K. Acharya, S. K. Bose, E. Galli, and S. A. Brown. Avalanches and criticality in self-organized nanoscale networks. *Science Advances*, 5(11), November 2019.
- [51] Xin Guo, Christina Schindler, Stephan Menzel, and Rainer Waser. Understanding the switching-off mechanism in Ag+ migration based resistively switching model systems. *Applied Physics Letters*, 91(13), September 2007.
- [52] L. Niemeyer, L. Pietronero, and H. J. Wiesmann. Fractal dimension of dielectric breakdown. *Physical Review Letters*, 52(12):1033–1036, March 1984.

SUPPLEMENTARY INFORMATION: TREE NETWORKS OF REAL-WORLD DATA: ANALYSIS OF EFFICIENCY AND SPATIOTEMPORAL SCALES

A PREPRINT

Davide Cipollini^{*,1,2}, Lambert Schomaker^{1,2}

¹ Bernoulli Institute for Mathematics, Computer Science and Artificial Intelligence,
University of Groningen, Nijenborgh 9, 9747 AG Groningen, The Netherlands

² Cognigron - Groningen Cognitive Systems and Materials Center,
Nijenborgh 9, 9747 AG Groningen, The Netherlands

*Corresponding author: Davide Cipollini Email: d.cipollini@rug.nl

Keywords Trees · Networks · Thermodynamics · Statistical physics · Machine Learning · von Neumann entropy · Specific heat

S1 Laplacian spectrum

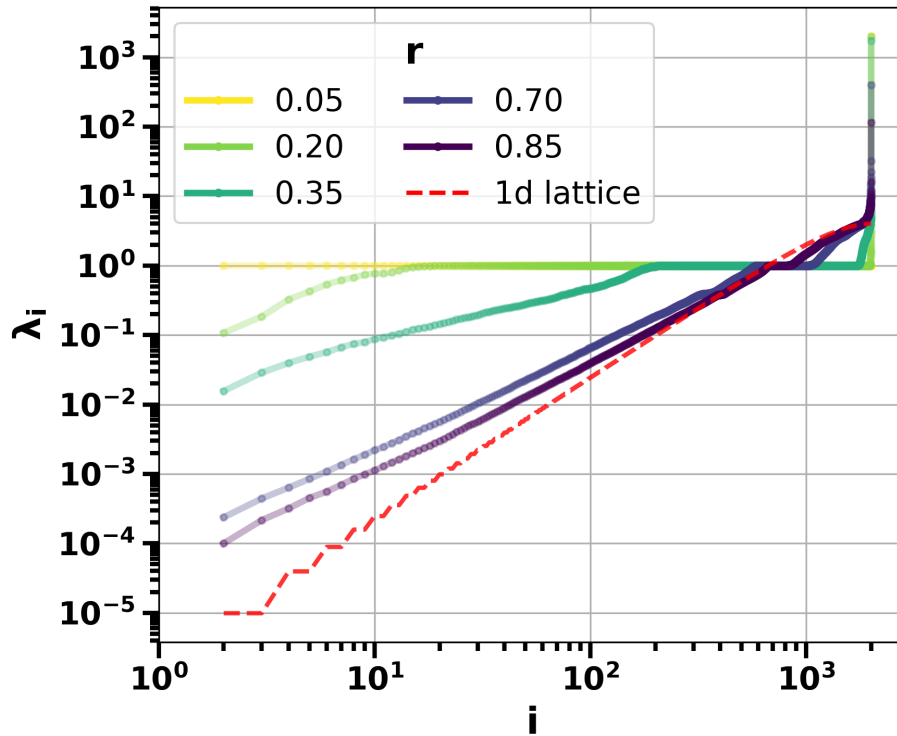


Figure S1: **Laplacian spectrum** for multiple values of r . The red dashed line indicates the limit of a 1-dimensional lattice. The greater the degeneracy in the eigenvalue spectrum the larger the peak in the specific heat (see Figure S6). For the case of the star graph $r = 0.05$ the maximum eigenvalue is equal to the maximum number of nodes $\lambda_{max} = 2000$. Points are averaged over 50 independent network generations from the subset of 2000 FashionMNIST samples.

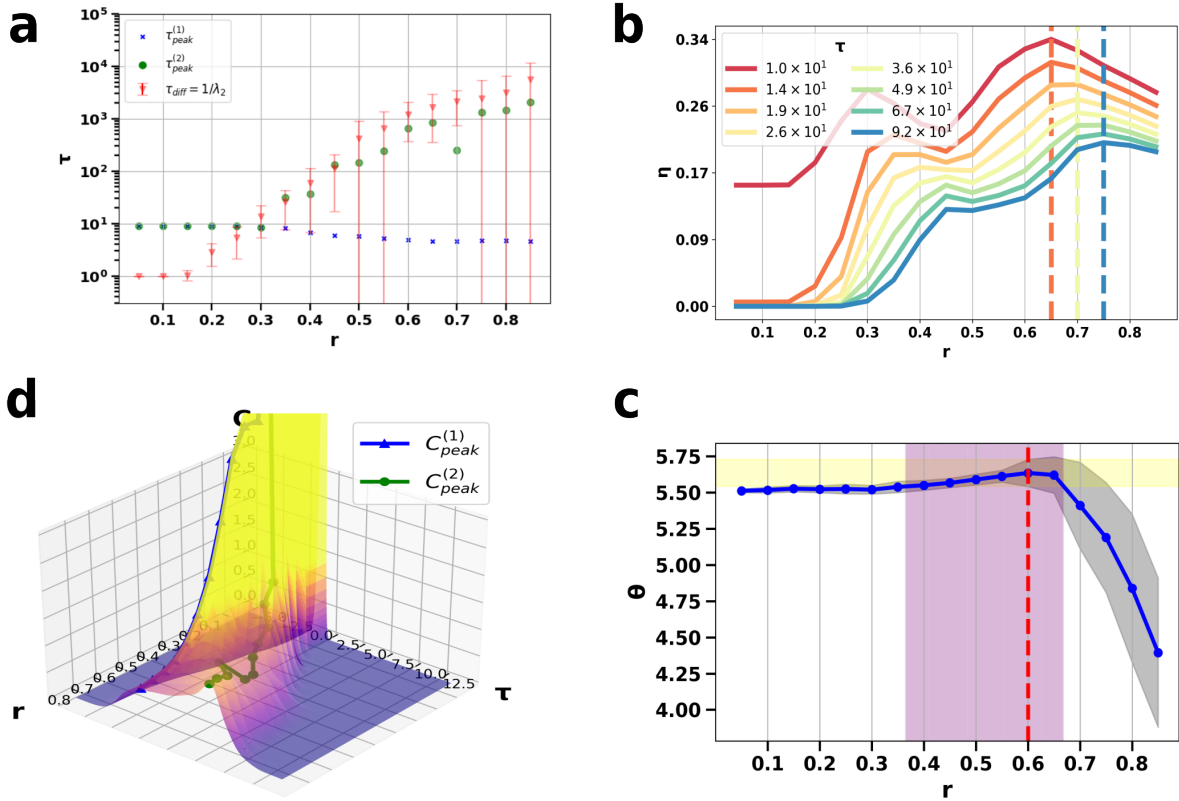
S2 Larger networks: N=4000


Figure S2: **MNIST - N=4000**. In (a) the bifurcation of $\tau_{peak}^{(1)}$ and $\tau_{peak}^{(2)}$ curves identify the τ -scale relevant for the topological transition. The jump of $\tau_{peak}^{(2)}$ towards $\tau_{peak}^{(1)}$ is less pronounced compared to networks of 2000 nodes. In red the numerical average of the diffusion time $1/\tau_{diff} = \lambda_2$ is plotted for reference, see the main text for discussion. In (d) the specific heat, C , the surface is illustrated. The $C_{peak}^{(1,2)}$ curves correspond to the specific heat values evaluated along the curves $\tau_{peak}^{(1,2)}$ in (a). In (b)-(c) the efficiencies η and θ are plotted as a function of r with the dashed lines indicating the global maxima. The η is computed in the τ -range of one order of magnitude from the τ -scale indicated by the bifurcation of $\tau_{peak}^{(1)}$ in (a). For larger networks N=4000 optimal r remains unchanged as it is a property mostly dependent on the dataset complexity. The shaded area in (c) spans over the two local maxima in panel (b) (see main text for discussion). Quantities are averaged over 50 independent simulations.

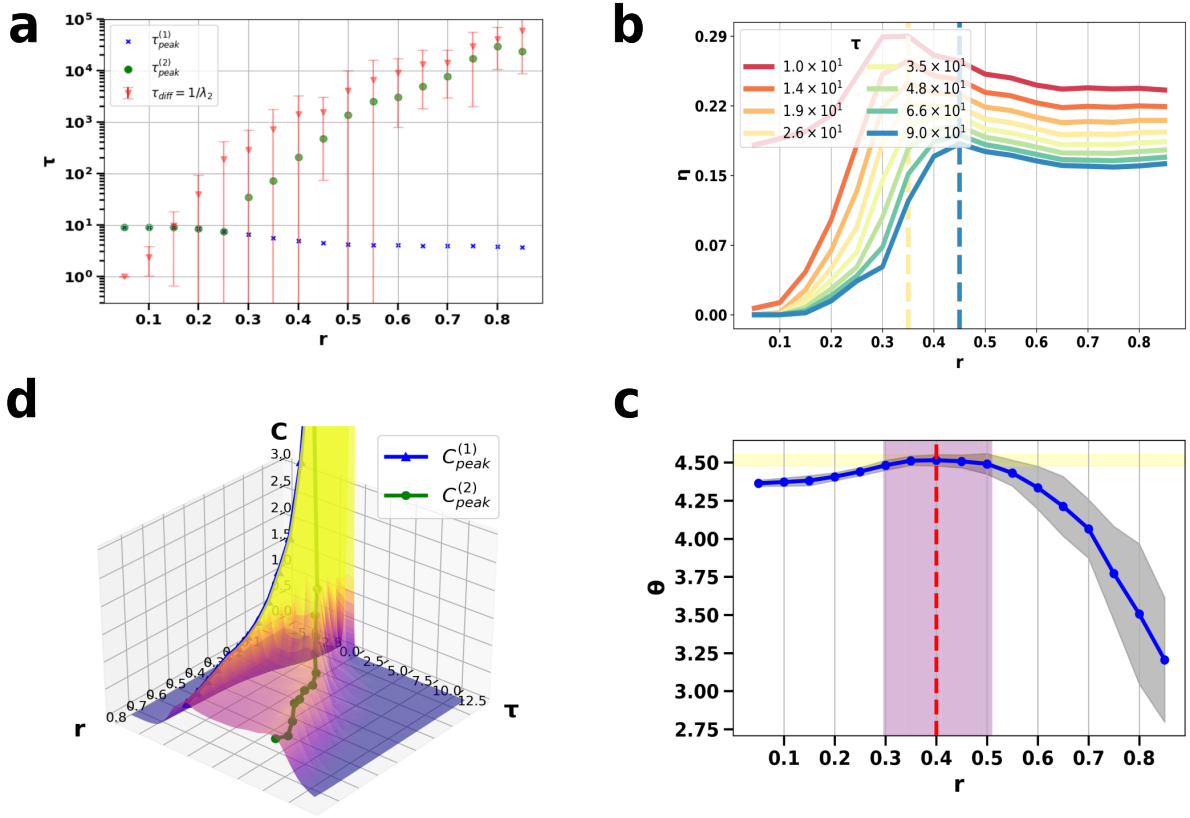


Figure S3: **FashionMNIST - N=4000**. In (a) the bifurcation of $\tau_{peak}^{(1)}$ and $\tau_{peak}^{(2)}$ curves identify the τ -scale relevant for the topological transition. The red curve depicts the numerical average of the diffusion time $1/\tau_{diff} = \lambda_2$, see the main text for discussion. In (d) the specific heat, C , the surface is illustrated. The $C_{peak}^{(1,2)}$ curves correspond to the specific heat values evaluated at $\tau_{peak}^{(1,2)}$ in (a). In (b)-(c) the efficiencies η and θ are plotted as a function of r with the dashed lines indicating the global maxima. The η is computed in the τ -range of one order of magnitude from the τ -scale indicated by the bifurcation of $\tau_{peak}^{(1,2)}$ in (a). Note that the maxima of the efficiencies is posited at the edge of the critical value of $r \sim 0.35$ indicating the FashionMNIST as a dataset more complex than the other two investigated, that does benefit from the critical region. Quantities are averaged over 50 independent simulations.

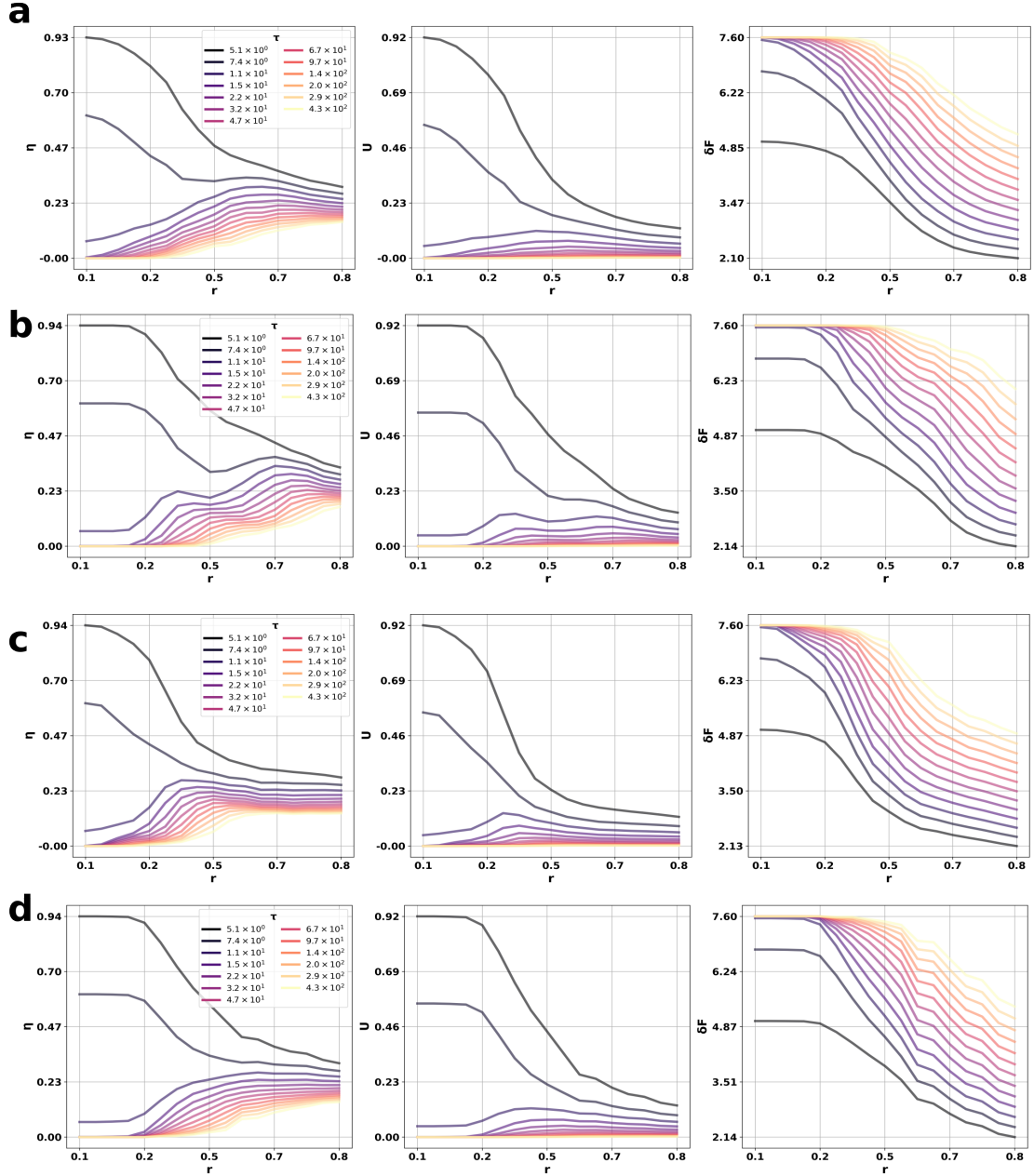
S3 $\eta, \mathbf{W}, \mathbf{U}$


Figure S4: $\eta, \mathbf{W}(= \delta F), \mathbf{U}$ for multiple resolution-scales τ . η changes concavity for smaller τ than the transition resolution scale and the coherence between thermodynamic and pattern-matching efficiency is lost for resolution τ -scales above and below the order of magnitude where the transition appears, i.e. $\tau \sim 10$. Panels **(a)-(d)** show the transition for trees of order $N = 2000$, hence 2000 samples from the datasets NIST, MNIST, FashionMNIST, and CIFAR10 respectively. Curves are averaged over 50 independent iterations.

S4 Von Neumann entropy and specific heat

Figures S5-S10 depict the spectral entropy, S in blue, and the specific heat, C in red, for multiple values of the control parameter r . Y-ticks on the right axis correspond to the theoretical specific heat plateau values for an infinite 2d-lattice, random tree, and 1-d lattice respectively in descending order.

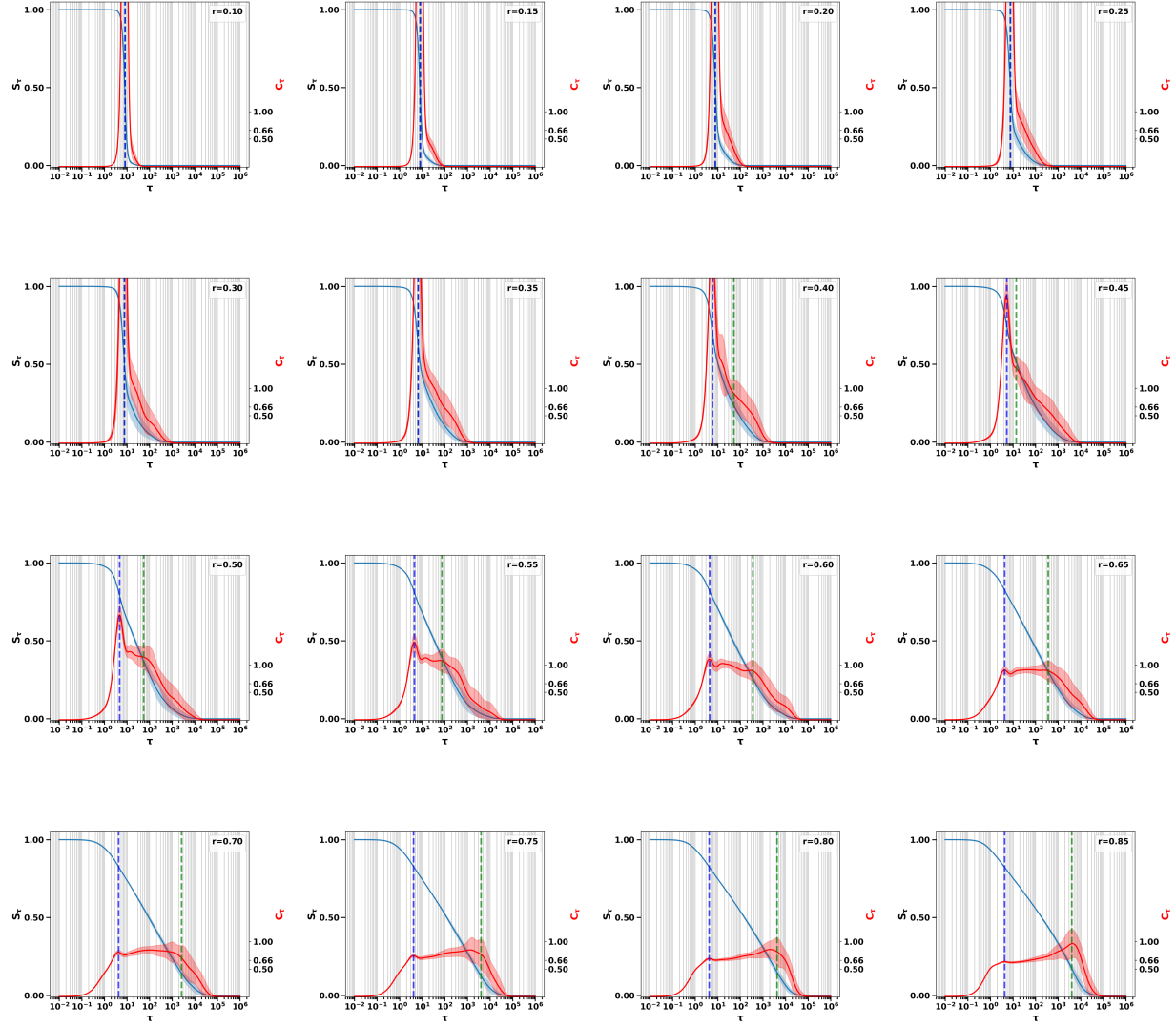


Figure S5: **Von Neumann and specific heat - NIST: 2000 samples.** The table shows the von Neumann entropy (blue) and the specific heat (red) for $r = \{0.10, \dots, 0.85\}$. Vertical dashed lines indicate the peaks corresponding to $\tau_{peak}^{(1)}$ (blue) and $\tau_{peak}^{(2)}$ (green) in the main text. Shaded areas represent the standard deviation. Curves are averaged over 50 simulations.

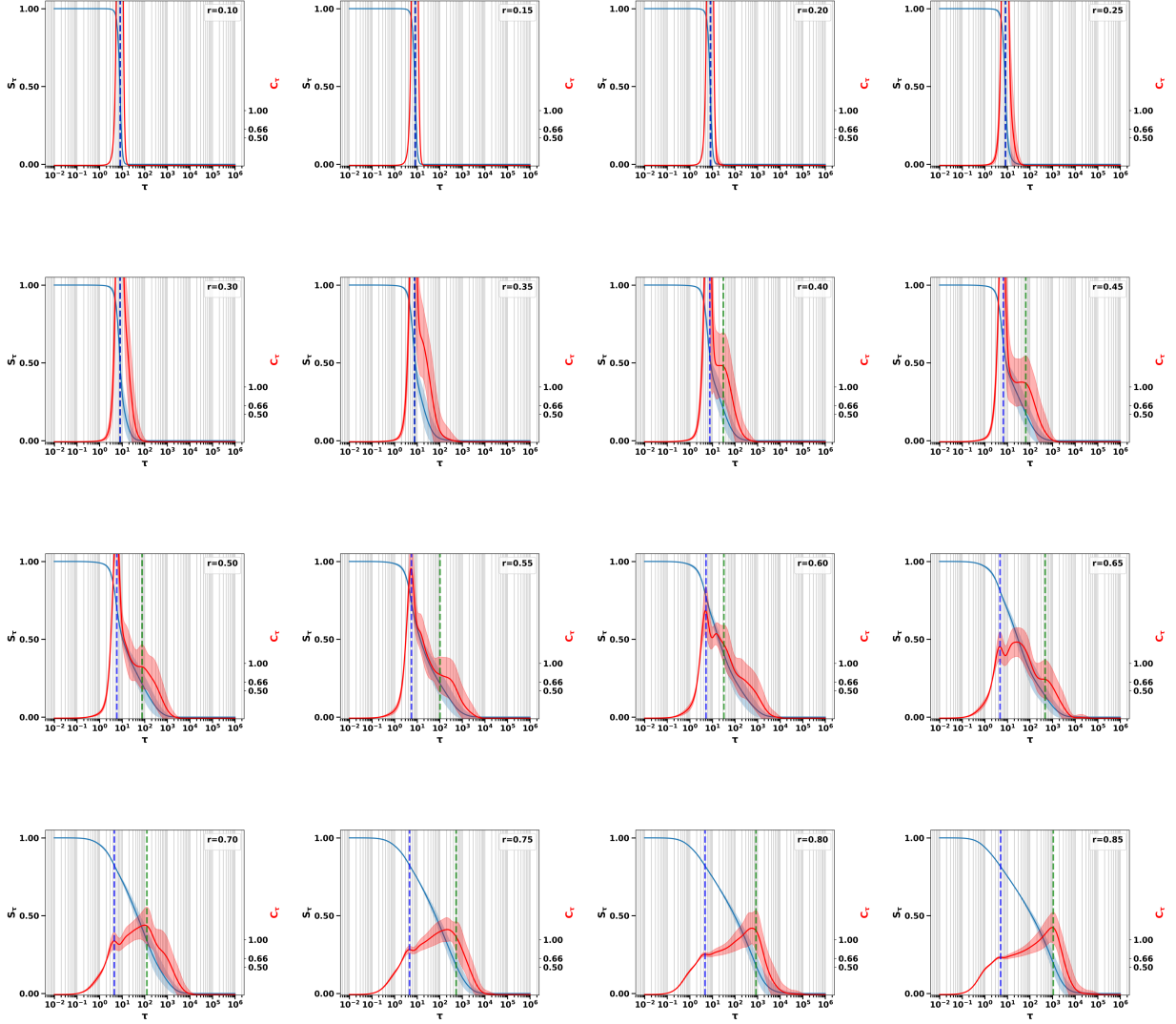


Figure S6: **Von Neumann and specific heat - MNIST: 2000 samples.** The table shows the von Neumann entropy (blue) and the specific heat (red) for $r = \{0.10, \dots, 0.85\}$. Vertical dashed lines indicate the peaks corresponding to $\tau_{peak}^{(1)}$ (blue) and $\tau_{peak}^{(2)}$ (green) in the main text. Shaded areas represent the standard deviation. Curves are averaged over 50 simulations.

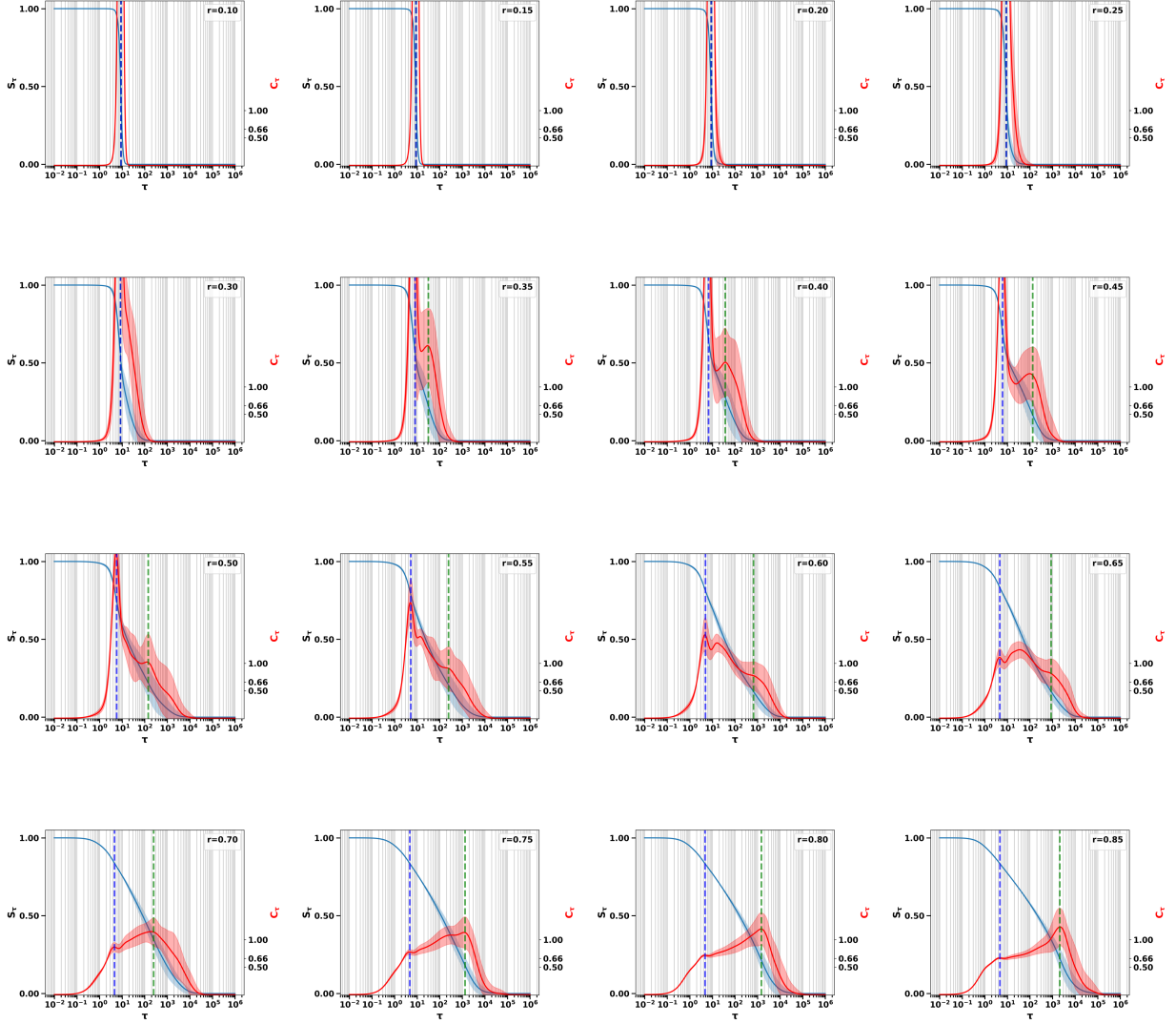


Figure S7: **Von Neumann and specific heat - MNIST: 4000 samples.** The table shows the von Neumann entropy (blue) and the specific heat (red) for $r = \{0.10, \dots, 0.85\}$. Vertical dashed lines indicate the peaks corresponding to $\tau_{peak}^{(1)}$ (blue) and $\tau_{peak}^{(2)}$ (green) in the main text. Shaded areas represent the standard deviation. Curves are averaged over 50 simulations.

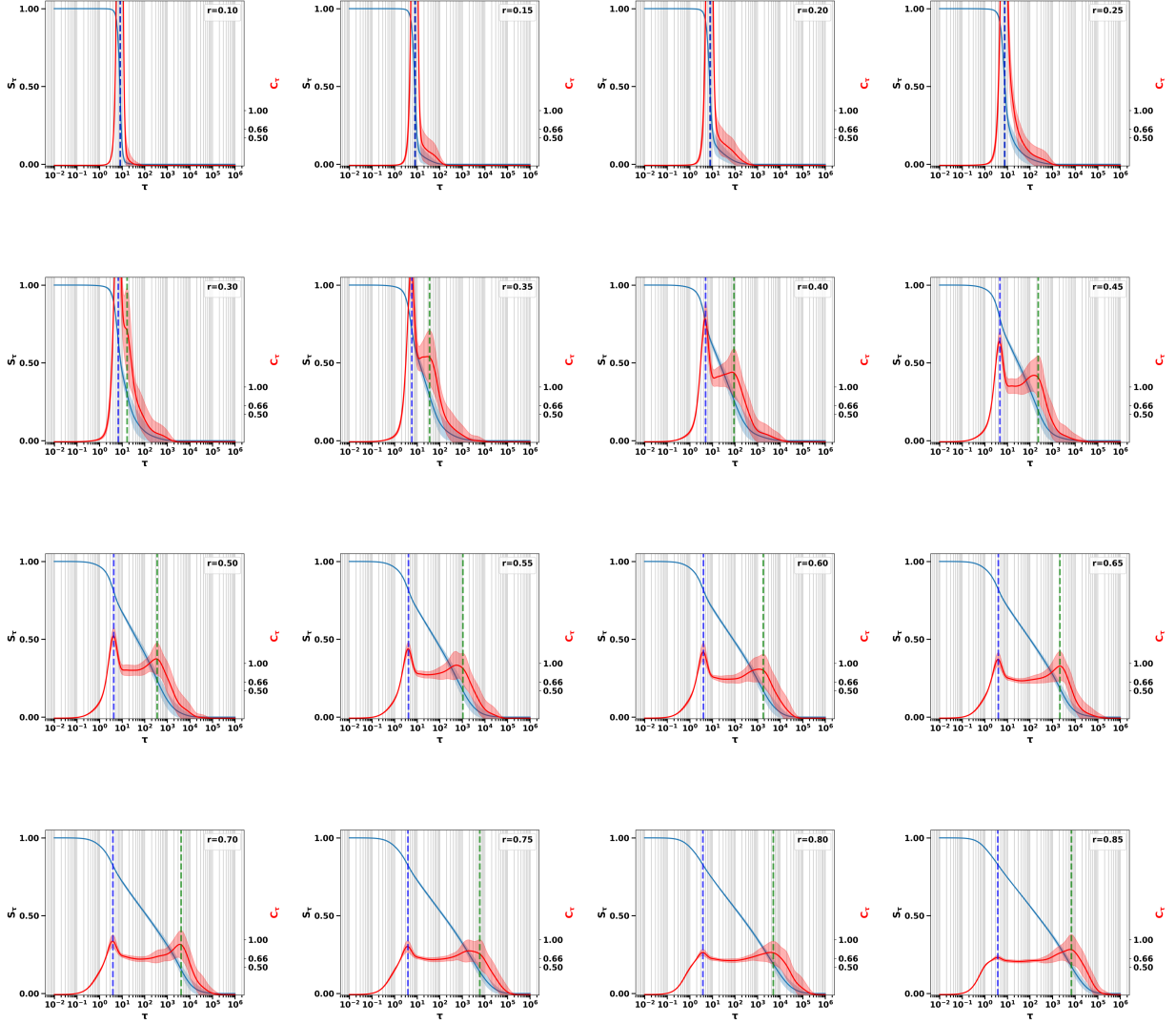


Figure S8: **Von Neumann and specific heat - FashionMNIST: 2000 samples.** The table shows the von Neumann entropy (blue) and the specific heat (red) for $r = \{0.10, \dots, 0.85\}$. Vertical dashed lines indicate the peaks corresponding to $\tau_{peak}^{(1)}$ (blue) and $\tau_{peak}^{(2)}$ (green) in the main text. Shaded areas represent the standard deviation. Curves are averaged over 50 simulations.

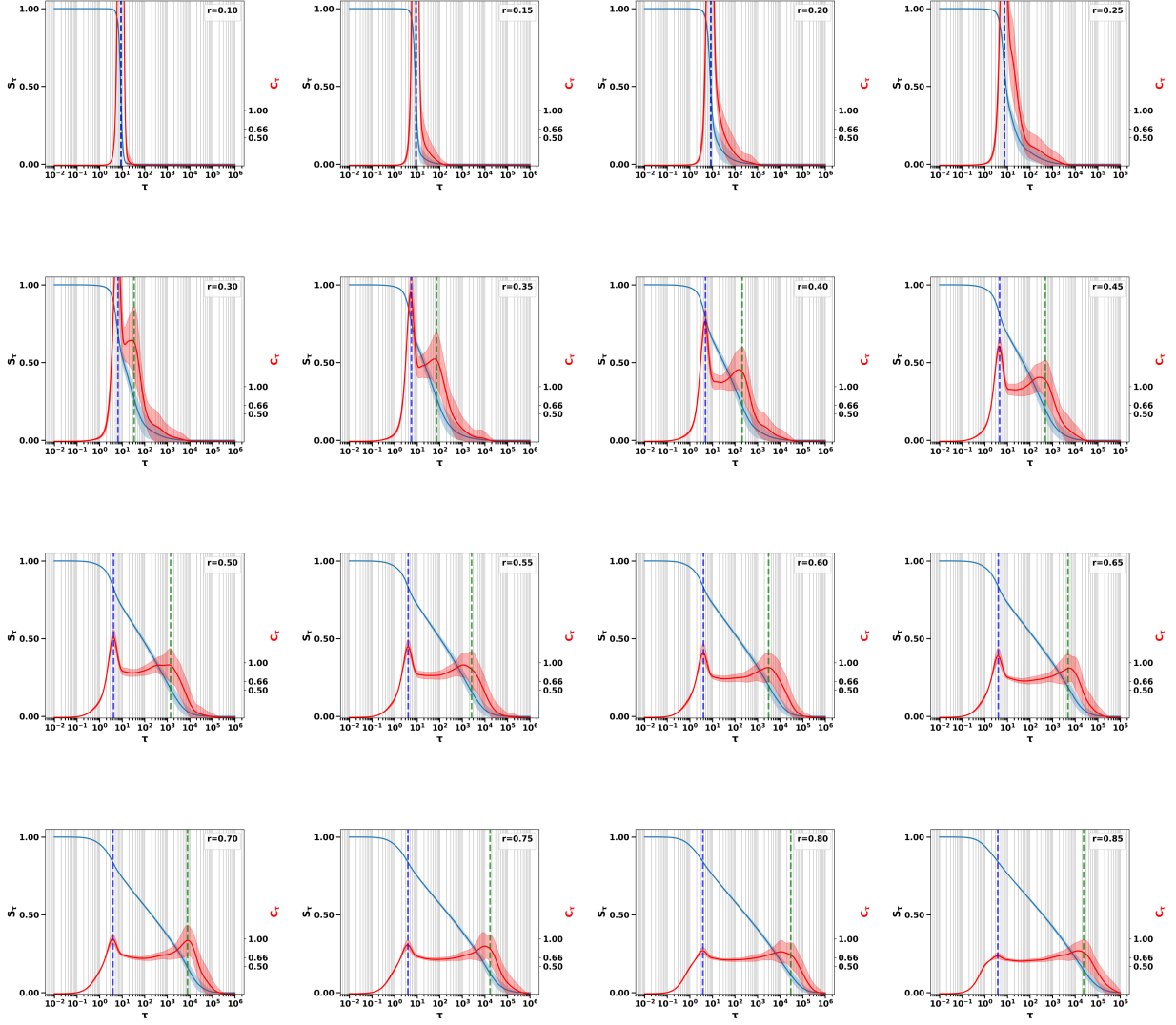


Figure S9: **Von Neumann and specific heat - FashionMNIST: 4000 samples.** The table shows the von Neumann entropy (blue) and the specific heat (red) for $r = \{0.10, \dots, 0.85\}$. Vertical dashed lines indicate the peaks corresponding to $\tau_{peak}^{(1)}$ (blue) and $\tau_{peak}^{(2)}$ (green) in the main text. Shaded areas represent the standard deviation. Curves are averaged over 50 simulations.

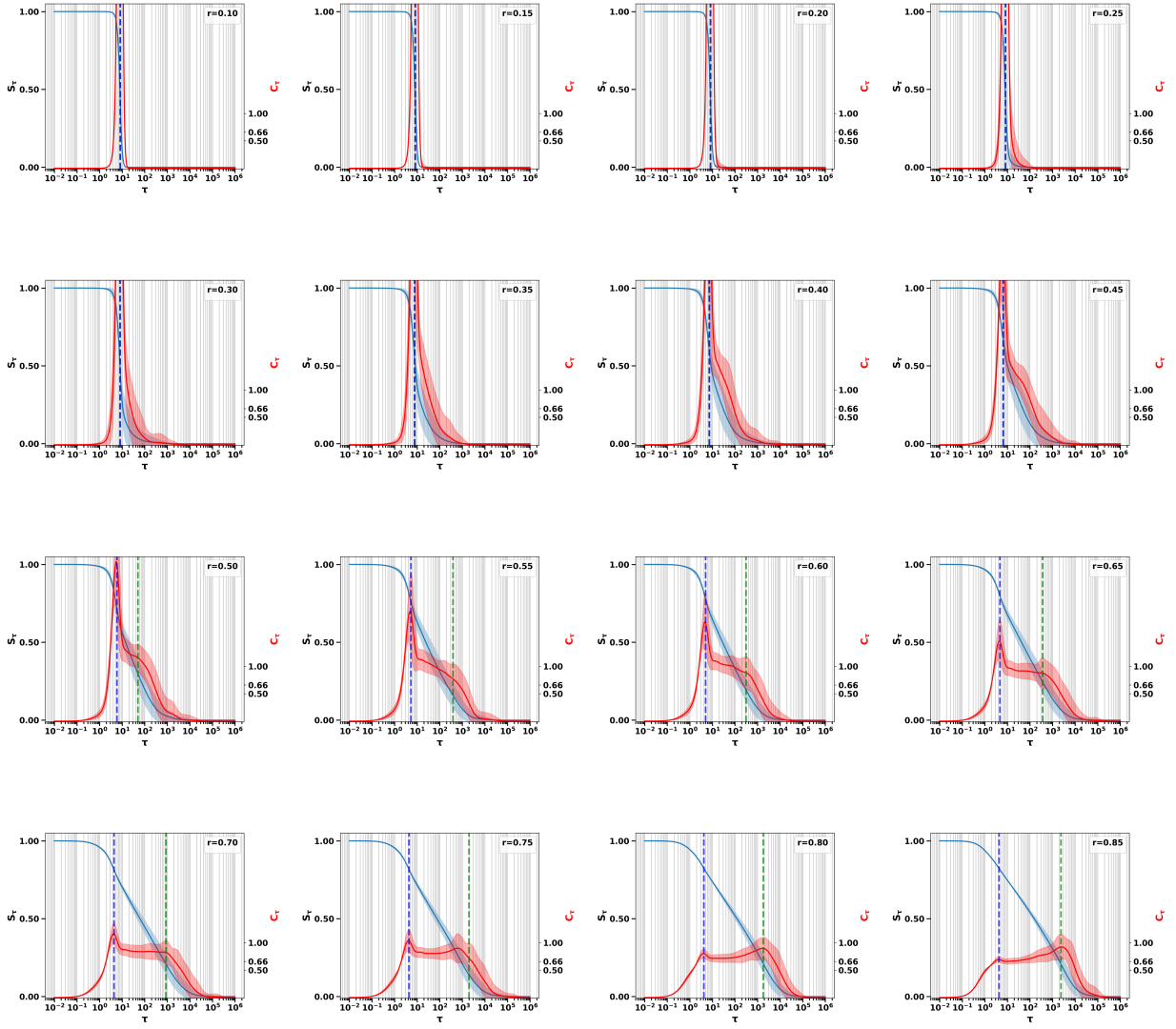


Figure S10: **Von Neumann and specific heat - CIFAR10: 2000 samples.** The table shows the von Neumann entropy (blue) and the specific heat (red) for $r = \{0.10, \dots, 0.85\}$. Vertical dashed lines indicate the peaks corresponding to $\tau_{peak}^{(1)}$ (blue) and $\tau_{peak}^{(2)}$ (green) in the main text. Shaded areas represent the standard deviation. Curves are averaged over 50 simulations.

S5 Variance of F , δF , δS , η

Figure S10 shows the variance of the quantities F , δF , δS , η for the three datasets. The peak of the variance indicates the location of the structural phase transition.

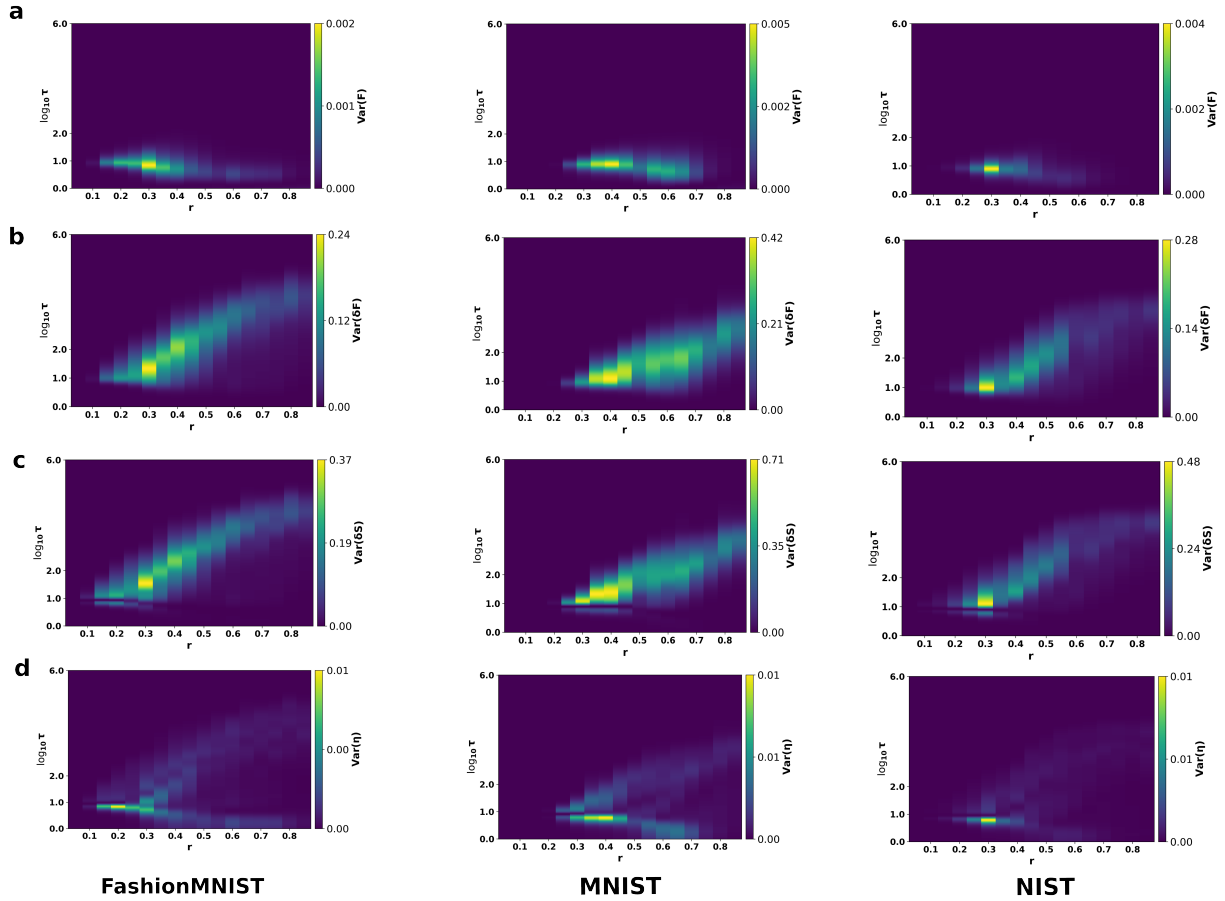


Figure S11: **Variance of F , δF , δS , η - 2000 samples** in panels (a) through (d) for the three datasets (columns). The peaks of the variance indicate the structural phase transition. Variance computed over 50 independent simulations.

S6 Variance of \hat{D} , \hat{L} , and S

Figure S11 shows the variance of the internal energy $U = \text{Tr}[\hat{\rho}\hat{L}] = \langle \hat{L} \rangle$, the ensemble degree $\langle D \rangle$ and the entropy S in panels (a), (b) and (c) respectively. Note that $\text{Var}(S) \propto C$. These figures highlight the observation expressed in the main text: the interesting scale for the computation of the efficiency is where the bifurcation in panel (c) appears while the interesting behavior of other quantities such as the efficiency in the main text or the ensemble degree are not necessarily observed at the r -values where the bifurcation appears.

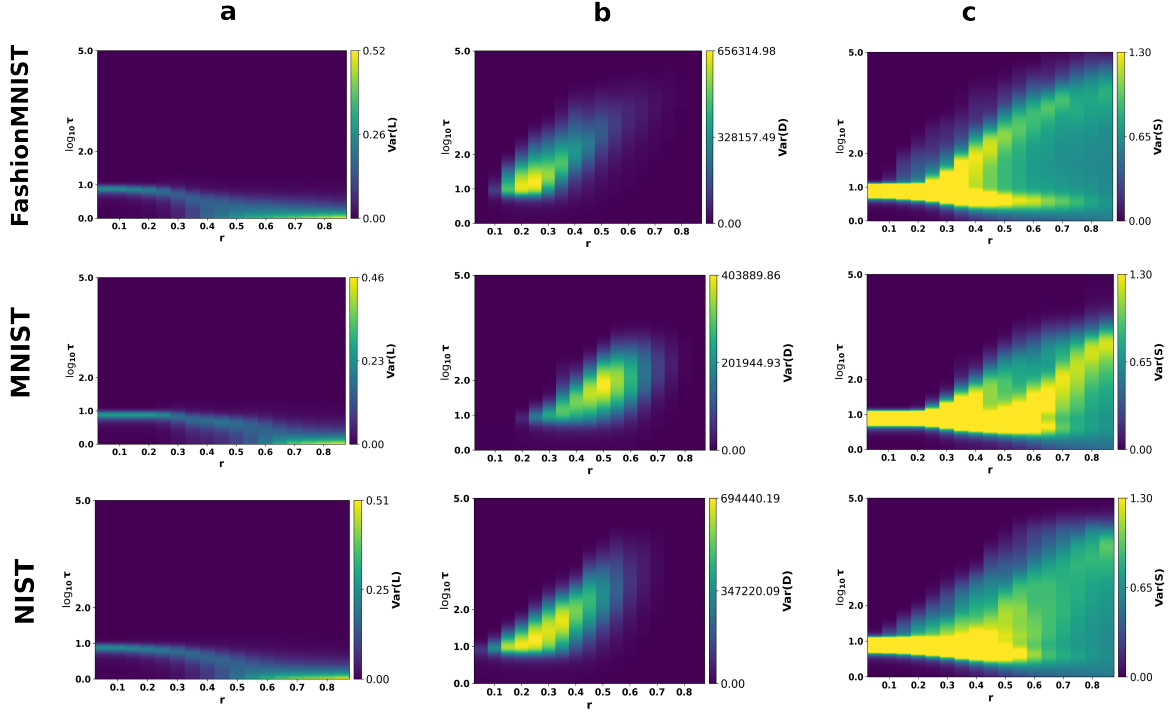


Figure S12: **Variance of \hat{D} , \hat{L} , and S - 2000 samples** in panels (a) through (c) respectively. It is interesting to note how the contributions to the bifurcation of the specific heat $C \propto \text{Var}(S)$ are decoupled by measuring the variance of the matrices \hat{L} and \hat{D} . In the main text $U = \text{Tr}[\hat{L}\hat{\rho}] = \langle \hat{L} \rangle$. The bifurcation of the s . Average over 50 simulations.

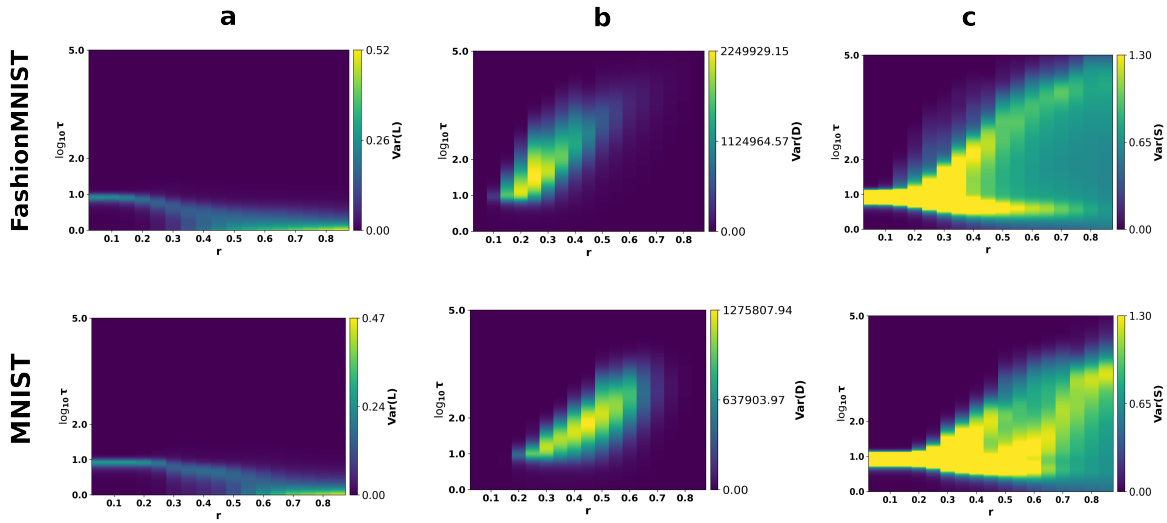


Figure S13: **Variance of \hat{D} , \hat{L} , and S - 4000 samples** in panels (a) through (c) respectively. It is interesting to note how the contributions to the bifurcation of the specific heat $C \propto Var(S)$ are decoupled by measuring the variance of the matrices \hat{L} and \hat{D} . In the main text $U = \text{Tr}[\hat{L}\hat{\rho}] = \langle \hat{L} \rangle$. Average over 50 simulations.

S7 Pattern-matching efficiency

In Figures S14 and S15 the accuracy, the (log)number of distances computed, and the pattern-matching efficiency θ are shown for the case of networks of 2000 and 4000 samples respectively, for the MNIST in the first and for the FashionMNIST in the second row of each figure.

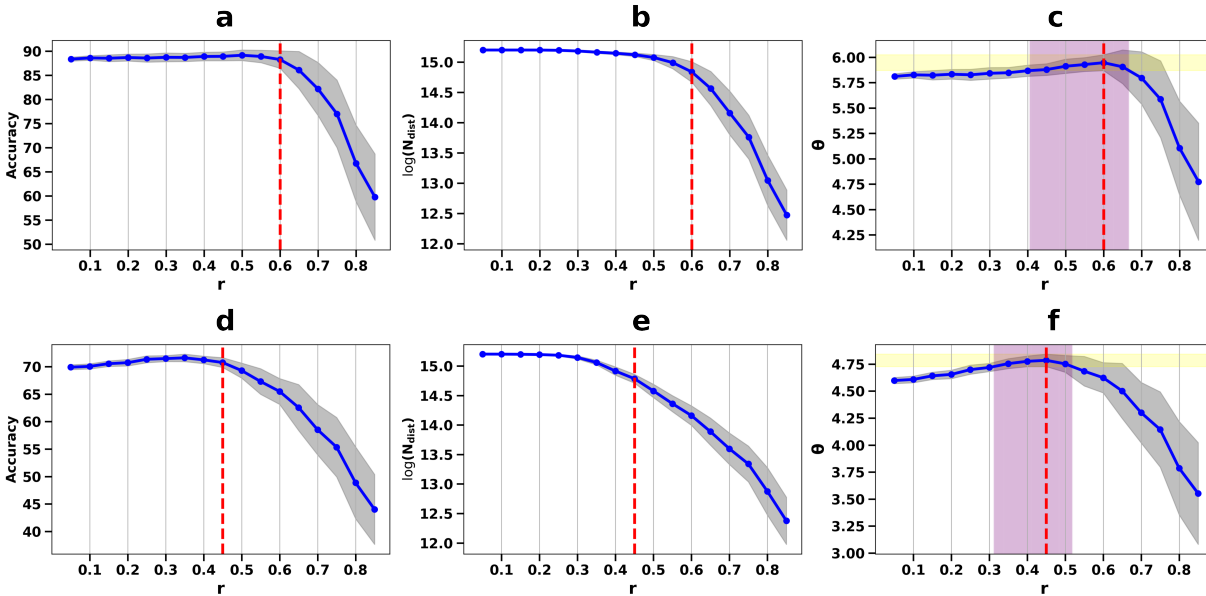


Figure S14: **Pattern-matching efficiency - 2000 samples** in (c, f) measured over the MNIST and FashionMNIST respectively. The efficiency θ is defined as the trade-off between the classification accuracy, (a, c), and the logarithm of the number of distances computed to find the best match, (b, e). The dashed-red vertical line indicates the optimal r value in terms of efficiency θ . The shaded grey area designates the standard deviation. The purple shaded area in panel (c, f) indicates a tolerance r -domain of optimal efficiency. The tolerance domain is defined as the r -values such that the corresponding θ -values are included in one standard deviation computed at the maximum θ , whose y-axis projection is indicated by the yellow shaded area. Curves are computed over 50 independent simulations with a subset of 2000 samples extracted from each dataset. The 10 classes are equally represented both in the train- and test sets.

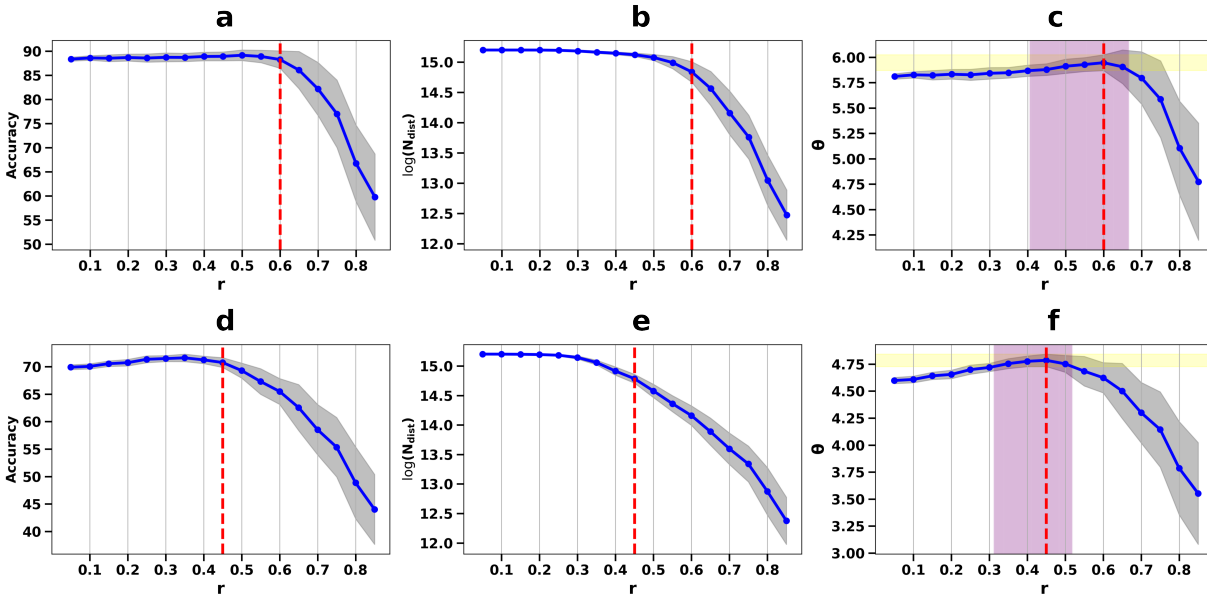


Figure S15: **Pattern-matching efficiency - 4000 samples** in (c, f) measured over the MNIST and FashionMNIST respectively. The efficiency θ is defined as the trade-off between the classification accuracy, (a, c), and the logarithm of the number of distances computed to find the best match, (b, e). The dashed-red vertical line indicates the optimal r value in terms of efficiency θ . The shaded grey area designates the standard deviation. The purple shaded area in panel (c, f) indicates a tolerance r -domain of optimal efficiency. The tolerance domain is defined as the r -values such that the corresponding θ -values are included in one standard deviation computed at the maximum θ , whose y-axis projection is indicated by the yellow shaded area. Curves are computed over 50 independent simulations with a subset of 2000 samples extracted from each dataset. The 10 classes are equally represented both in the train- and test sets.

Author Contributions

DC: Theoretical framework, Conceptualization, Methodology, Simulations, Data curation, Software, Writing – original draft, Writing – review & editing. LS: Writing – review & editing, Conceptualization, Supervision, Funding acquisition.

Funding

This work was funded by EUs Horizon 2020, from the MSCA-ITN-2019 Innovative Training Networks program "Materials for Neuromorphic Circuits" (MANIC) under the grant agreement No. 861153, as well as by the financial support of the CogniGron research center and the Ubbo Emmius Funds (Univ. of Groningen).

Acknowledgments

We are thankful to Jos van Goor for providing some of the scripts that enabled efficient grid-search across parameters and to Federico Balducci for the useful discussions.

Data Availability Statement

The original contributions presented in the study are included in the article/supplementary material, further inquiries can be directed to the corresponding author/s. Datasets and scripts can be found at https://github.com/CipolliniDavide/Laplacian_Trees.